THEORETICAL AND MATERIAL STUDIES ON THIN-FILM ELECTROLUMINESCENT DEVICES

Third Six-Monthly Report for the Period
1 April 1986 - 30 September 1986

Project No. A-4168

Prepared for:
Dr. J.B.Robertson/494
NASA
Langley Research Center
Hampton, VA 23665

Prepared by:
Dr. C.J. Summers* and Dr. K.F. Brennan+
Georgia Institute of Technology
Atlanta, GA 30332

December 1986

*Georgia Tech Research Institute and Microelectronics Research Center

+School of Electrical Engineering and Microelectronics Research Center

Introduction

During this report period work has progressed on theoretical investigations of the use of superlattices for promoting the efficiency of electroluminescent devices and the MBE growth of ZnS on GaAs and Si substrates. The first of these investigations has been prepared for publication and is presented in the following section. The MBE growth activities as described in section 2.

The Variably Spaced Superlattice Electroluminescent Display: A New High Efficiency Electroluminescence Scheme

K. F. Brennan[1]
and
C. J. Summers[2]

Microelectronics Research Center
Georgia Institute of Technology
Atlanta, Georgia 30332

Abstract

We present a new, highly efficient DC electroluminescent display. A variably spaced superlattice structure is used to produce high energy injection of electrons into a ZnSe:Mn active layer in which impact excitation of the Mn centers can occur. The device is predicted to operate at an applied external bias on order of magnitude less than the best DC electroluminescent device to date. The device is predicted to have comparable brightness, since it operates in the saturation regime. The improved efficiency stems from avoiding significant energy loss to phonons. The electrons sequentially tunnel through a multilayer ZnSe/$CaSrF_2$ stack under bias and emerge into the active layer at an energy equal to the conduction band bending. The injection energy is chosen to coincide with the impact excitation energy of the Mn centers. Different device designs are presented and their performance is predicted.

---

[1]School of Electrical Engineering

[2]Georgia Tech Research Institute

1. Introduction

The vast majority of computer terminal displays are presently made with cathode ray tubes, CRTs. CRTs are reliable, inexpensive, high quality visual color displays. However, CRTs have limited usefulness in lightweight, portable terminals owing to their large size, fragility, and high voltage requirements. Alternatively, flat panel displays, such as electroluminescent, liquid crystal and plasma displays, are being developed for lightweight, portable computer terminals. Each of these emerging technologies, in turn, has its own limitations. Liquid crystal displays, though they provide high quality resolution at low power requirements, only emit a single color. Plasma displays can be made to emit different colors, but at present these displays are prohibitively expensive. Present electroluminescent, EL, devices consume much power and, thereby, require high voltage drive sources. However, EL displays can be made to emit in different colors and can be reliably manufactured. Therefore, at present, none of the three technologies has clearly emerged as the successor to the CRT [1].

Electroluminescent displays are presently very inefficient in terms of power output and brightness versus electrical power input. The basic EL mechanisms are low field, minority carrier injection as in light emitting diodes, and high field acceleration of majority carrier electrons to optical energies at which luminescent centers can be impact excited [2,3]. High field EL was first reported in ZnS [4] and since has been investigated in a host of new materials as an application of new thin film technology [5-10]. Two basic device schemes have been realized to date using AC and DC power supplies, respectively.

AC electroluminescent devices are made by encapsulating a large band gap semiconductor, such as ZnS:Mn or ZnSe:Mn, by two insulating layers, typically Y_2O_3, on either side of the semiconductor layer. An AC bias is applied across the device which alternately accelerates the electrons from one semiconductor/insulator interface to the other. The source of the charge carriers is believed to be the interface states which exist between the semiconductor and insulator layers [2,3]. Due to the relatively small number of interface states, the free carrier distribution is quite small, $< 1.0 \times 10^{11}$ $1/cm^3$ [3]. Electroluminescence occurs when the free carriers are accelerated to sufficiently high energy such that impact excitation of the Mn centers is possible. The probability of an electron impact exciting a center depends upon the collision cross section, the density of centers in the semiconductor layer, and the probability of an electron achieving the impact excitation threshold energy.

DC electroluminescent devices, first reported by Thornton [11], have been realized using metal-insulator-semiconductor, M-I-S, metal-insulator-metal, M-I-M, structures or Schottky barriers [12,13]. In these devices, the source of free charge carriers is the metal electrode. Through application of a reverse bias in a Schottky barrier device, electrons tunnel from the metal into the semiconductor. Similar tunneling of electrons through a very narrow insulator layer in M-I-S devices leads to significant carrier injection. The principle advantage of DC electroluminescent devices over their AC counterparts is due to the much larger free carrier concentration within the DC device available to impact excite the luminescent centers, i.e., Mn or comparable rare earths in the ZnS or ZnSe layers.

DC EL devices are operated in two different modes, continuous and pulsed. Pulsed operation typically results in longer device lifetimes at the same brightness levels as compared to continuous operation [12]. Nevertheless, performance deterioration with time is a critical disadvantage of DC EL devices. The deterioration in continuous DC devices is due to the increase in resistivity which can be partially offset through pulsed operation [12]. Resistive deterioration does not occur in AC devices since they are capacitive structures. Additional advantages of DC over AC EL devices are lower power consumption, more versatility in shape and size, and ease of construction [12].

At present all electroluminescent devices suffer from poor power efficiencies, i.e., 0.1% for DC EL devices [12]. The poor device efficiencies appear to be due to several factors, difficulty in heating sufficient carriers to energies high enough to impact excite the centers, small collisional cross sections for excitation, and limited center concentrations due to quenching effects [2]. The main requirements for a center are inner shell transitions well shielded from the applied electric field, isovalent or neutral to avoid drift aided diffusion of the centers (this is of greatest importance in the DC devices since the field always points in the same direction), large cross section for impact excitation, high solubility, high radiative efficiency within the center, and emission within the visible spectrum [2]. To date the center identified with the most favorable qualities is Mn within either ZnS or ZnSe. In light of the restraints upon the center, it is difficult to improve upon either the excitation cross section, an intrinsic property of the center itself, or upon the doping concentration of centers (at high concentrations of Mn, quenching [2] occurs, reducing performance). Consequently, efficiency

enhancement can best be achieved by increasing the number of hot electrons available within the semiconductor layer.

The most obvious means of increasing the hot electron concentration is by application of a high electric field across the semiconductor layer. In steady state, the carrier heating from the field is balanced on average by inelastic scattering processes. The principle scattering processes which act to relax the energy of the distribution are phonon scattering, impact ionization, and in the case of EL devices, impact excitation. Both impact ionization and excitation are threshold processes in that the carriers must achieve sufficient energy in order to initiate the process. In a wide band gap semiconductor such as ZnSe or ZnS, extremely high electric fields must be applied to heat the electrons to sufficient energies in order to affect impact excitation of luminescent centers. The maximum electric field that can be applied, though, is limited by the onset of drift aided diffusion of the excitation centers and ultimately by dielectric breakdown of the semiconductor itself. Therefore, few electrons survive from field heating alone to high energies at which impact excitation can occur, resulting in very low efficiency operation of existing EL devices.

It is instructive to analyze the nature of the electron distribution function in a typical wide band gap semiconductor such as ZnSe under the application of an applied electric field. The competing processes of field heating and phonon energy relaxation result in only a very small fraction of the electrons attaining high energies. For purposes of illustration, the steady state electron energy distribution is calculated using an ensemble many particle Monte Carlo simulation [14,15] which includes the full details of the first and second conduction bands in ZnSe derived from an empirical pseudo-

potential calculation [16]. The calculation includes a full description of the electron-phonon scattering processes as treated using collisional broadening [17], as well as the impact ionization process using the Keldysh formulation [18]. The calculation assumes a "soft" impact ionization threshold based on the assumption that the ionization rate in ZnSe is much less than in a more narrow band gap semiconductor such as GaAs. A future paper will treat the high energy transport properties of ZnSe and ZnS, steady state drift velocities, and impact ionization rate in much closer detail.

The distribution function at several applied electric fields, 500.0, 700.0, and 1000.0 kV/cm, is presented in Figure 1. As can be seen from Figure 1, at each applied electric field, the high energy tail of the distribution is quite small. The probability of an electron drifting to an energy at or above the excitation energy, ~2.3 eV for Mn centers, is low even at 1000.0 kV/cm. In order to impact excite a center, an electron must have an energy greater than or equal to the excitation energy. At energies above 2.7 eV, impact ionization competes with the impact excitation to cool the carrier distribution.

As mentioned above, the efficiency ratio of input power to output power (brightness) can best be improved through producing more high energy carriers within a narrow energy range near the excitation energy. An efficient means of injecting carriers at high energy is through use of a heterojunction [19]. The injection energy is provided by the potential energy offset, due to the conduction band edge discontinuity between two adjacent semiconductor layers. The realization of a heterojunction discontinuity of ~2.3 eV at a ZnS or ZnSe interface is totally impractical since the band gaps of these materials are extremely large. Consequently, a novel means is necessary to provide high

energy injection of electrons into either ZnS or ZnSe to promote impact excitation of the luminescent centers. We propose herein a new superlattice injection scheme using a variably spaced superlattice [20], which provides efficient high energy injection of carriers in a sharp distribution centered around the impact excitation energy of the luminescent center.

2. Device Scheme and Model Description

As discussed above, the most obvious means of heating the free carrier distribution in a semiconductor is through the application of an electric field. Under steady state conditions, field heating is balanced on average by competing phonon cooling events which determine the average energy of the distribution. Fluctuations from the average energy, arising from carriers gaining more energy from the field than is lost to the phonons, occur over small lengths of time. These carriers, which deviate from the average ensemble behavior, constitute the high energy tail of the distribution function and produce impact excitation events. In order to greatly enhance the number of carriers in the high energy tail of the distribution, a means of defeating the phonon cooling process, even over only a short distance or length of time, is necessary.

Three methods have recently been disclosed which provide means of locally heating the electron distribution functions well above the quasi-steady state average energy. Local electron heating can be accomplished through use of potential step discontinuities as in multiquantum well/superlattice structures [21,22], by use of a built-in electric field arising from a fully depleted p-i-n or p-n junction in conjunction with a band edge discontinuity [23-27], or by use of resonant tunneling in a superlattice structure [20,28]. In all

of these structures, the electron energy distribution function is greatly heated so as to effect a large enhancement in the electron impact ionization rate, a threshold process similar to the impact excitation process.

Electroluminescent devices are unipolar. Since no holes are present in the device, one is concerned only with engineering the conduction band through the use of multiquantum wells and superlattice schemes. The variably spaced superlattice scheme [20] provides a means of selectively heating the electron energy distribution through conduction band edge engineering. Figure 2 illustrates the basic operation of the variably spaced superlattice. The superlattice is designed such that under reverse bias the levels in each quantum well become resonantly aligned. This provides a resonant tunneling channel through the superlattice. Owing to the conduction band bending, due to the applied electric field, the electrons are then injected into the active semiconductor layer (ZnSe doped with Mn centers) at extremely high energies with respect to the conduction band minimum. In this way, the electron energy distribution is locally heated to an energy centered on the impact excitation energy of the luminescent center.

The basic EL device scheme is composed of either one stage or stages of unit cells containing a variably spaced superlattice immediately followed by an active semiconductor layer. The overall bias supplied must be sufficiently large to resonantly align each superlattice. Any residual bias is dropped across the semiconductor layers producing an electric field within the layers.

The device geometry, potential barrier widths and heights and quantum well widths, is determined using an exact solution of the sequential resonant tunneling problem in multilayered structures under bias [28,29]. The transmissivity of the structure is determined as a function of the incident

electron energy using the transfer matrix approach. The well and barrier widths are adjusted such that under the bias corresponding to the desired electron injection energy, ~2.5 eV in the case of Mn centers in ZnSe, a resonant tunneling channel occurs at low energies. Therefore, electrons near the fermi energy in a metal contact to the left of the superlattice can resonantly tunnel through the structure and emerge at an energy ~2.5 eV.

3. Device Design and Performance

The proposed device consists of two separate regions, a variably spaced superlattice made from ZnSe lattice matched to the $CaSrF_2$ ternary compound, and a ZnSe:Mn active layer. The variably spaced superlattice provides for high energy electron injection, ~2.5 eV, into the active layer in which impact excitation of the Mn luminescent centers can occur. The voltage drop across the superlattice therefore must remain fixed at ~2.5 volts. However, the voltage drop within the active layer can be controlled by doping the ZnSe layer accordingly. We present below different designs for both regions, the superlattice and the active region, and estimate the relative improvement in luminescent efficiency over devices using bulk ZnSe:Mn layers.

The design of the superlattice region is obtained based on an exact solution of the sequential resonant tunneling problem under bias [28]. The device can only be designed by recursively calculating the transmissivity until apparent alignment of the resonance peaks, corresponding to the confined quantum states, occurs. The sequential tunneling calculation is necessary since it includes the effects of coupling between the quantum states. Decoupled treatment of the quantum wells incorrectly predicts the energy resonances. The energy of the resonance is most sensitive to the widths of

the individual quantum wells. Increasing the well widths acts to lower the confined states energy levels, while decreasing the widths raises the energy levels. Near resonant alignment of a three well, four barrier variably spaced $ZnSe/CaSrF_2$ superlattice is presented in Figure 3. In calculating the transmissivities, different electron effective masses have been assumed within the barriers and the wells, 0.17 and 0.5, respectively. The effective mass in $CaSrF_2$ is only a very rough approximation since very little information is available about this compound.

The effect of the potential barrier heights on the transmission coefficients and resonances is presented in Figure 4. The potential barrier heights are all taken to be 4.0 eV which results in decreased coupling and transmissivity. In addition, the levels shift upwards in energy. This is as expected since as the depth of any quantum well increases, the energy levels arising from spatial quantization effects within it increase.

Decreased coupling and transmissivity also occurs in structures in which the barrier widths are increased. Figure 5 illustrates the effect on the transmissivity of increased barrier widths. As is apparent from a comparison of Figures 3 and 5, the first resonance disappears entirely. It is important to realize that increasing the barrier widths at constant bias acts to reduce the effective electric field within the structure. A more accurate determination of the influence of the barrier widths on the resonances can be attained by adjusting the bias such that the field remains constant throughout the superlattice. Figure 6 plots the transmissivity as a function of incident carrier energy under constant electric field for a 25 Å barrier width device. Interestingly, the resonances are all split further apart and are shifted upwards in energy than those in Figure 3.

The three well, four barrier device of Figure 3 requires extremely small quantum well widths, as well as a very high electric field. In general, this scheme must be considered impractical from a materials growth point of view. A more practical device structure can be realized by aligning the first two $n = 1$ levels with the $n = 2$ quantum level in the third well. Such a structure is presented in Figure 7. This structure has the advantages of not only less stringent materials growth requirements but also operating at a lower electric field.

Another obvious way of reducing the electric field is to simply increase the number of wells used in the device. Figure 8 shows a four well, five barrier device design which also provides 2.5 eV injection. As in the case of the three well device of Figure 3, the well dimensions cannot be considered practical. Other device designs of four or more wells using higher order quantum levels can certainly be made. Unfortunately, the design of these structures is difficult since it requires repeated iterative calculations of the transmissivities. The procedure we have adopted is as follows. A three well structure is first studied to identify the nature of each resonance, i.e., which quantum level, $n = 1,2,3,\ldots$, in which quantum well, first, second, etc. In order to bring the levels into alignment, first the well widths are varied accordingly. If the level must be lowered in energy, the corresponding well width is widened. Conversely, if the level must be raised in energy, the corresponding well width is decreased. The barrier widths and heights are adjusted in order to increase the transmission, smaller barrier heights and widths act to increase the transmissivity. However, as seen from comparing Figures 3, 4, and 5, it is apparent that the barriers also influence the energies of the resonance. As pointed out above, as the barrier width is

changed, the effective electric field within the structure changes unless the bias is adjusted accordingly. In the device application of interest here, the injection energy is a design constraint. Therefore, the operating bias is not a freely adjustable parameter. Consequently, changes in the barrier widths require additional changes in the well widths. The strong interaction amongst the quantum levels then acts to greatly complicate the analysis of the structure. Further work is underway to find a more efficient means of predicting the resonant alignments as a function of the well widths, barrier heights, and barrier widths.

It is important to determine the optimal electric field within the active layer under which the impact excitation of the luminescent centers will be most effective. As mentioned above, the effective electric field within the active region can be engineered by adjusting the resistance through doping. The electron energy distribution function as a function of elapsed travel time has been calculated under the initial condition of 2.5 eV injection at various applied electric field strengths. The calculations are made using the ensemble Monte Carlo method described above. The effect of the electric field on the weighted distribution (includes the effect of the density of states) is presented in Figures 9-14. Electric field strengths varying from 10 to 1000 kV/cm are considered. The necessary doping is easily determined from the effective field strength as,

$$Nd = \frac{(F\ell + V)}{qA\mu FR_1} \qquad (1)$$

where F is the electric field in the active region, ℓ is the length of the active region, V is the total external bias applied, q is the electron charge,

A is the cross sectional area, and R_1 is the resistance of the SL (which is easily calculated from the potential drop of 2.5 volts divided by the current flow obtained from the transmissivity plots).

As can be seen from Figures 9 and 10, at low field strength the energy distribution relaxes quickly to lower energies. The "bunching up" of the distribution at 1.50 eV is due to the relatively small intervalley scattering rate between L and Γ. Many of the electrons are scattered into the L valley following the high energy injection. The field heating is insufficient to maintain the high average energy of the distribution. Therefore, since the intervalley relaxation rate back to gamma is not very strong, owing to the small density of states in gamma, the distribution tends to collapse towards the intervalley threshold energy, 1.50 eV. Some of the electrons remain in the Γ valley after injection and thermalize through polar optical emission events. These electrons have a high velocity. Consequently, the mean distance traveled by the electrons is much farther than if all of them are transferred into the subsidiary valleys.

As the applied electric field is increased, the distribution remains hotter over a longer duration, Figures 11-14. Many more carriers stay centered about the excitation energy. It is expected then that the impact excitation rate will greatly increase as the number of incident carriers centered about the collisional excitation energy increases. Table 1 shows the percentage of the electrons within the collisional excitation range, 2.5 to 2.1 eV, as a function of electric field and resulting total external bias (sum of the voltage drop within the active layer and across the superlattice region). It is interesting to note that as the field increases above 500 kV/cm, the distribution is again greatly cooled due to extensive impact

ionization, even after only 0.3 psec of travel time. There exists a tradeoff in the value of the electric field within the active region; too small a field results in rapid cooling of the distribution, while too large a field results in extensive impact ionization and subsequent cooling. From examination of Table 1 and Figures 9-14, it appears that the optimal electric field within the active region lies within the field range of 100-500 kV/cm.

The important question still remains; how does the proposed device compare to existing DC EL devices made from ZnSe:Mn? The critical issue, of course, is the relative efficiencies of the devices which are best measured in terms of the ratio of the output power (brightness) versus the input electrical power (energy needed to produce luminescence in the device). Ohnishi et al. [9] have recently reported a highly efficient bright green DC EL display using ZnSe. Their optimal device requires a driving voltage of ~60 volts. According to our projections in Table 1, the driving voltage per stage necessary in the SL device, of 500 Å width active layer, is roughly an order of magnitude less.

Use of a much lower applied DC bias is critical, not only from an efficiency standpoint but also from a device lifetime point of view. DC EL devices have long been known to suffer brightness deterioration under continuous operation [9]. The deterioration results mainly from the occurrence of nonemissive points. The dark spots result from thermal breakdown caused by extremely high current flow through a weak spot in the active layer [9]. Therefore, if the voltage drop is less throughout the active layer, less IR heating occurs within weak spots thereby extending the lifetime of the device.

The output brightness of the device is best experimentally measured. Experimental work is presently underway to first grow and measure the proposed device. In the absence of experimental measurements, the relative efficiency of the proposed device to standard devices using bulk ZnSe:Mn serves as the best performance measure of the proposed structure. There are two ways of calculating the impact excitation frequency within the device structure. From use of the Monte Carlo method and knowledge of the collisional cross section as a function of incident electron energy, the impact excitation rate can be determined similar to the approach used for impact ionization [14]. This approach relies entirely upon the accuracy with which the collisional probability can be assessed. In principle, the collisional probability can be determined from a calculation of the quantum mechanical matrix element as has been done for the impact ionization process [30-31]. The collisional excitation case though is radically different from the impact ionization process in that the transition occurs only over a relatively sharp energy range, that corresponding to the optical transition in the Mn atom. A future work will address this problem more fully. Alternatively, the excitation frequency can be estimated from the following

$$1/\tau \sim f(v,\theta,\phi)\ V\ N\ \sigma(\theta,\theta')\ d\Omega' \qquad (2)$$

where $f(v,\theta,\phi)$ is the distribution function, v is the average electron velocity, N is the number of target centers, and $\sigma(\theta,\theta')$ is the collisional cross section as a function of angle. If we assume a 1% Mn concentration (1% has been shown experimentally to give the maximum brightness [2]) and a saturation velocity of $\sim 1.0 \times 10^7$ cm/sec, equation (2) becomes,

$$1/\tau \sim 4 \times 10^{11} \int f(v,\theta,\phi)\, d\Omega' \qquad (3)$$

Finally, if both $f(v,\theta,\phi)$ and $\sigma(\theta,\theta')$ are taken to be isotropic, the impact excitation frequency becomes,

$$1/\tau \sim 5.0 \times 10^{12}\, \bar{f} \qquad 1/\text{sec} \qquad (4)$$

where $\bar{f}$ is the average normalized distribution function centered about the excitation energy, 2.5 to 2.1 eV. Since we only need compare between devices, the actual number of carriers does not enter into the calculation. All that is important is the relative number of electrons capable of impact exciting the luminescent centers. From Figure 1, $\bar{f}$ can be estimated in ZnSe at steady state conditions under an applied field of 1000 kV/cm to be (take the area under the curve between 2.5 and 2.1 eV), 0.045 or 4.5%. From Table 1, at 300 kV/cm, the values of $\bar{f}$ at 0.1, 0.2, and 0.3 psec of travel time are 71.2%, 29.4%, and 19.0%. Clearly, the proposed device dramatically increases the number of excitation events over those devices using high electric field excitation within bulk ZnSe.

The total number of excitation events, of course, depends upon the integrated probability, averaging of the distribution over the full transit distance of the active layer. This cannot be readily performed correctly, since after an excitation event occurs the incident electron no longer is available to excite another center, which is not taken into account in the above. Clearly, the Monte Carlo procedure discussed above is the best means of estimating the excitation frequency. Nevertheless, the above graphically illustrates the importance of the variably spaced superlattice device.

4. Conclusions

We have presented a new EL device which provides for efficient, high energy injection of electrons into an active layer (region doped with luminescent centers) through the use of a variably spaced superlattice. The device is predicted to operate at an applied external bias an order of magnitude less than the best EL device to date. The improved efficiency stems from the fact that the electron distribution is heated by sequential resonant tunneling through a multilayer ZnSe/$CaSrF_2$ stack. The electrons emerge from the superlattice at an energy equal to the band bending of the conduction band. Due to the quantized energy levels within the superlattice, the vast majority of carriers transit the structure without suffering significant phonon cooling. In contrast, existing DC EL devices require extremely high applied biases to heat sufficient carriers to the excitation energy since competing phonon cooling events occur. The proposed superlattice device defeats phonon cooling in heating the distribution.

The device design can be split into two separate issues, the design of the superlattice and the active layer. Use of higher quantum levels, n = 2,3, etc., is necessary in order to design a multilayer stack capable of being realized experimentally. In addition, multiple well designs, four or more wells, can be used.

The improvement in the excitation frequency over that in standard DC devices has been demonstrated. It is expected that the brightness levels will be comparable (most DC devices saturate in brightness as the number of incident electrons of sufficient energy becomes equal to the number of luminescent centers) in the proposed device, but at much lower bias requirements.

Acknowledgements

The authors would like to thank Dr. J. Robertson for helpful discussions. The technical assistance of P. Knight and D. Fouts at the Georgia Institute of Technology is gratefully appreciated. This work was sponsored by NASA under grant NAG-1-586.

Figure Captions

Figure 1: Calculated electron energy distribution function in bulk ZnSe at three different electric field strengths, 500, 700, and 1000 kV/cm respectively. The distribution function is weighted by the density of states function.

Figure 2: Schematic representation of the variably spaced superlattice scheme. a) Device geometry; b) zero bias; c) applied bias, $eV \sim E_1$.

Figure 3: Logarithm of the transmissivity as a function of the incident electron energy for a three well, four barrier $ZnSe/CaSrF_2$ variably spaced superlattice. The resonances corresponding to the confined quantum states in the wells are resonantly aligned at low energy providing a tunneling channel for high energy injection.

Figure 4: Logarithm of the transmissivity as a function of the incident electron energy for a three well, four barrier $ZnSe/CaSrF_2$ variably spaced superlattice as described in the drawing. Note that in this case, all of the barrier heights are 4.0 eV as compared to those in Figure 3. Physically, the wells become less coupled, the transmissivity decreases (structure becomes more opaque) and the resonances occur at higher energies in accordance with the behavior of confined states in quantum wells.

Figure 5: Logarithm of the transmissivity as a function of the incident electron energy for the three well structure presented in Figure 3, but with 25 Å barrier widths. Again, notice that the coupling between the resonances is reduced, as witnessed by the spreading of the resonance peaks. The first resonance disappears entirely.

Figure 6: Logarithm of the transmissivity as a function of the incident electron energy for the three well structure considered in Figure 5. In this case, the bias is adjusted such that the effective electric field is identical to that of the device in Figure 3. It is apparent that widening the barriers results in extensive decoupling of the resonances.

Figure 7: Logarithm of the transmissivity as a function of the incident electron energy for a three well, four barrier structure using the n = 2 quantum level in the third well. The distinct advantage of this design is the relaxed constraints on the materials growth technology in addition to lower field operation.

Figure 8: Logarithm of the transmissivity as a function of the incident electron energy for a four well, five barrier ZnSe/$CaSrF_2$ structure. The interaction between the resonances is such that closer resonant alignment is not possible. The particular advantage of this structure is that a much lower electric field is required for 2.5 eV injection than in the three well structure. Twenty angstrom (20 Å) width barriers are chosen to reduce the coupling and, hence, repulsion between the levels.

Figure 9: Calculated electron energy distribution function in ZnSe following 2.5 eV injection at a field strength of 10 kV/cm.

Figure 10: Calculated electron energy distribution function in ZnSe following 2.5 eV injection at a field strength of 30 kV/cm.

Figure 11: Calculated electron energy distribution function in ZnSe following 2.5 eV injection at a field strength of 100 kV/cm.

Figure 12: Calculated electron energy distribution function in ZnSe following 2.5 eV injection at a field strength of 300 kV/cm.

Figure 13: Calculated electron energy distribution function in ZnSe following 2.5 eV injection at a field strength of 500 kV/cm.

Figure 14: Calculated electron energy distribution function in ZnSe following 2.5 eV injection at a field strength of 1000 kV/cm.

References

[1] T. S. Perry and P. Wallich, IEEE Spectrum, 22, 52 (1985).

[2] R. Mach and G. O. Muller, Phys. Stat. Sol. (a), 69, 11 (1982).

[3] F. Williams, J. of Luminescence, 23, 1 (1981).

[4] G. Destriau, J. de Chemie Physique, 33, 620 (1936).

[5] R. Mach, W. Gerricke, H. Treptow, and W. Ludwig, Phys. Stat. Sol. (a), 49, 667 (1978).

[6] D. C. Morton and F. E. Williams, Appl. Phys. Lett., 35, 671 (1979).

[7] K. Okamoto and Y. Hamakawa, Appl. Phys. Lett., 35, 508 (1979).

[8] J. Benoit, P. Benalloul, R. Parrot, and J. Matther, J. of Luminescence, 18/19, 739 (1979).

[9] H. Ohnishi, H. Yoshino, K. Ieyasu, N. Sakuma, and Y. Hamakawa, Proceedings of the SID, 25/3, 193 (1984).

[10] F. J. Bryant, A. Krier, and G. Z. Zhong, Solid-State Electronics, 28, 847 (1985).

[11] W. A. Thornton, J. Appl. Phys., 30, 123 (1959).

[12] A. Vecht, N. J. Werring, R. Ellis, and P. J. F. Smith, Proceedings of the IEEE, 61, 902 (1973).

[13] H. Matsumoto, S. Tanaka, and T. Yabumoto, Jap. J. of Appl. Phys., 17, 1543 (1978).

[14] H. Shichijo and K. Hess, Phys. Rev. B, 23, 4197 (1981).

[15] K. Brennan, T. Wang, and K. Hess, IEEE Electron Dev. Lett., EDL-6, 199 (1985).

[16] M. L. Cohen and T. K. Bergstresser, Phys. Rev., 141, 789 (1966).

[17] Y. C. Chang, D. Z.-Y. Ting, J. Y. Tang, and K. Hess, Appl. Phys. Lett. 42, 26 (1983).

[18] L. V. Keldysh, Zh. Eksp. Teor. Fiz., 48, 1692 (1965) [Sov. Phys.-JETP, 21, 1135 (1965)].

[19] J. Y. Tang and K. Hess, IEEE Trans. Electron Dev., ED-29, 1906 (1982).

[20] C. J. Summers and K. F. Brennan, Appl. Phys. Lett., 48, 806 (1986).

[21] R. Chin, N. Holonyak, Jr., G. E. Stillman, J. Y. Tang, and K. Hess, Electron. Lett., 16, 467 (1980).

[22] F. Capasso, W. T. Tsang, and G. F. Williams, IEEE Trans. Electron. Dev., ED-30, 381 (1983).

[23] H. Blauvelt, S. Margalit, and A. Yariv, Electron. Lett., 18, 375 (1982).

[24] K. Brennan, IEEE J. Quantum Electron., QE-22, 1999 (1986).

[25] K. Brennan, to be published in IEEE Trans. Electron. Dev.

[26] K. Brennan, unpublished.

[27] K. Brennan, unpublished.

[28] K. F. Brennan and C. J. Summers, to be published in J. of Appl. Phys.

[29] C. J. Summers, K. F. Brennan, H. D. Rogers, and B. K. Wagner, to be published in Microstructures and Superlattices.

[30] A. S. Kyuregyan, Fiz. Tekh. Poluprovoch., 10, 690 (1976); Sov. Phys. Semicond., 10, 410 (1976).

[31] J. T. Devreese and R. G. van Welzeris, Appl. Phys. A, 29, 125 (1982).

Table 1

Comparative Device Efficiencies as a Function of Applied Field for a 500 Å Wide Active Layer Width

Elapsed Time (psec)	Mean Distance (Å)	% Carriers Within 2.5 to 2.1 eV
(1) F = 10 kV/cm; Total Bias = 2.55 volts		
0.1	108.5	71.9
0.2	168.0	22.4
0.3	244.0	8.4
0.4	343.0	4.7
0.5	461.0	3.2
steady state	---	0.0
(2) F = 30 kV/cm; Total Bias = 2.65 volts		
0.1	140.0	73.3
0.2	185.0	24.7
0.3	258.0	26.2
0.4	366.0	5.7
0.5	450.0	3.0
steady state	---	0.0
(3) F = 100 kV/cm; Total Bias = 3.0 volts		
0.1	74.0	79.3
0.2	121.0	30.0
0.3	178.0	12.0
0.4	270.0	6.8
0.5	353.0	3.9
steady state	---	0.0
(4) F = 300 kV/cm; Total Bias = 4.0 volts		
0.1	84.0	71.2
0.2	135.0	29.4
0.3	188.0	19.0
0.4	250.0	11.9
0.5	302.0	8.1
steady state	---	0.3

Table 1 (Continued)

Elapsed Time (psec)	Mean Distance (Å)	% Carriers Within 2.5 to 2.1 eV
(5) F = 500 kV/cm; Total Bias = 5.0 volts		
0.1	66.2	64.6
0.2	130.0	45.0
0.3	186.0	26.0
0.4	264.0	19.0
0.5	323.0	14.6
steady state	---	2.5
(6) F = 1000 kV/cm; Total Bias = 7.5 volts		
0.1	80.0	25.5
0.2	144.0	17.3
0.3	197.0	13.1
0.4	256.0	12.8
0.5	302.0	11.5
steady state	---	4.5

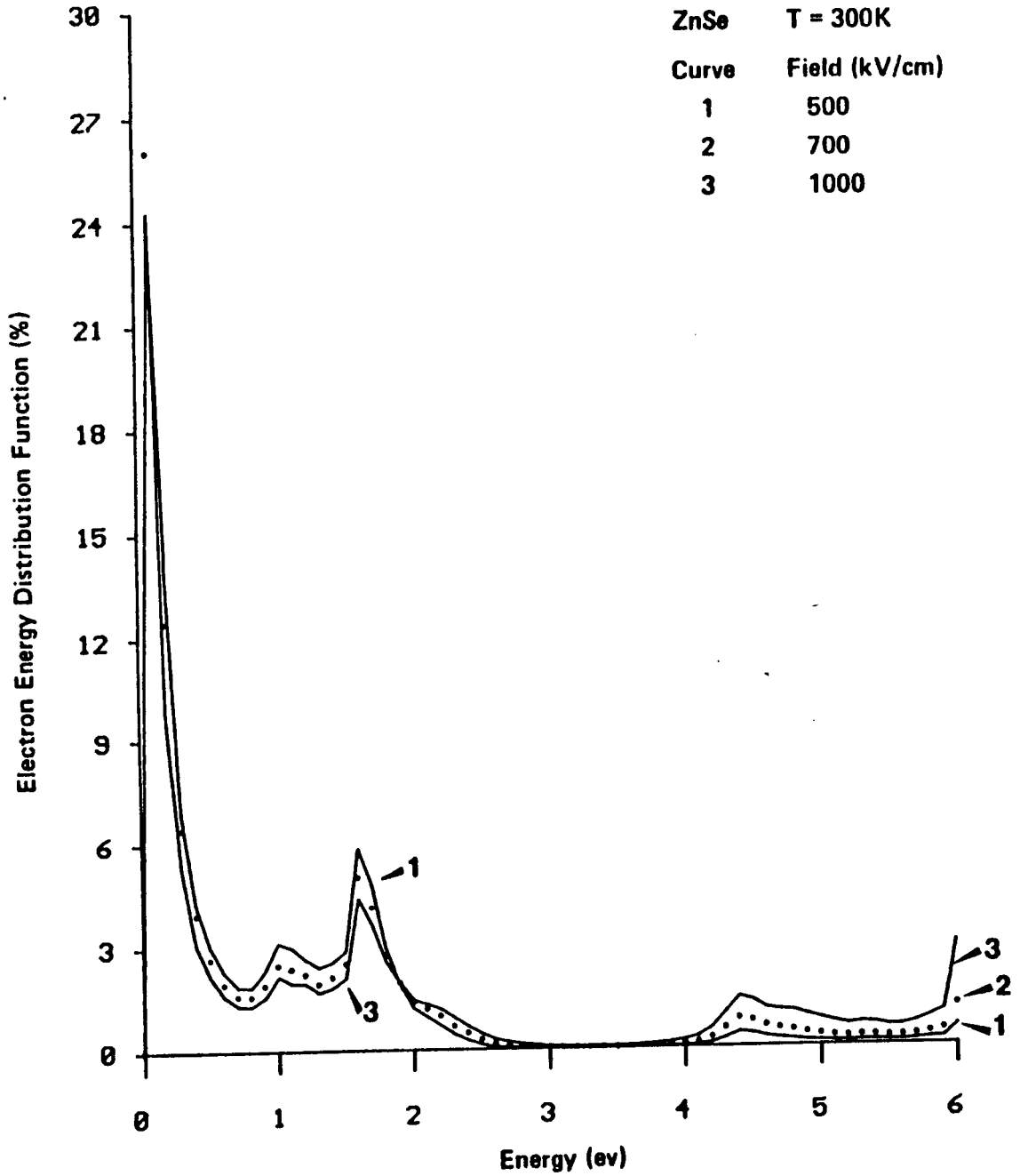

Fig. 1
Brennan: Summers

(a)

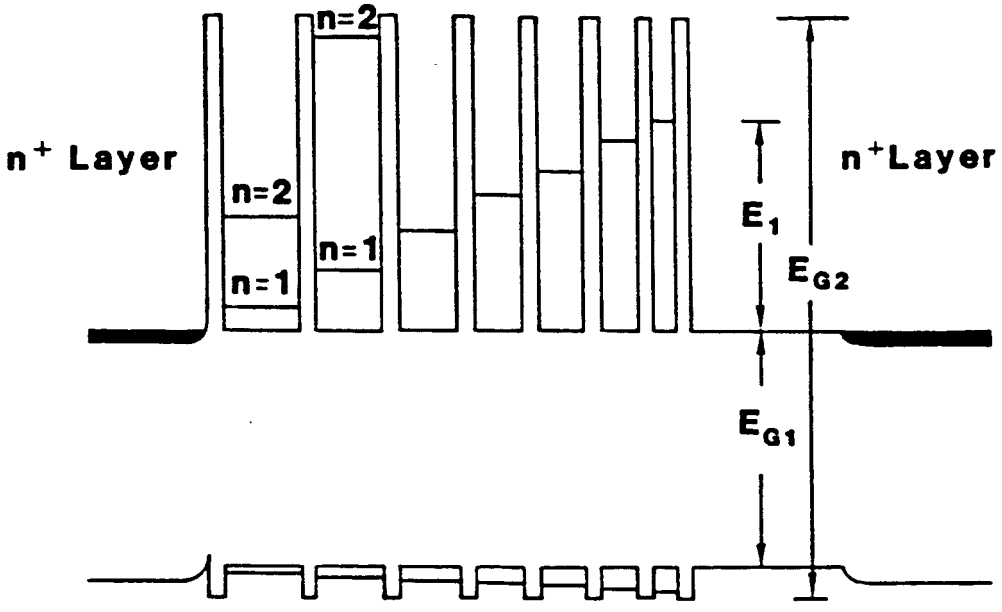

(b)

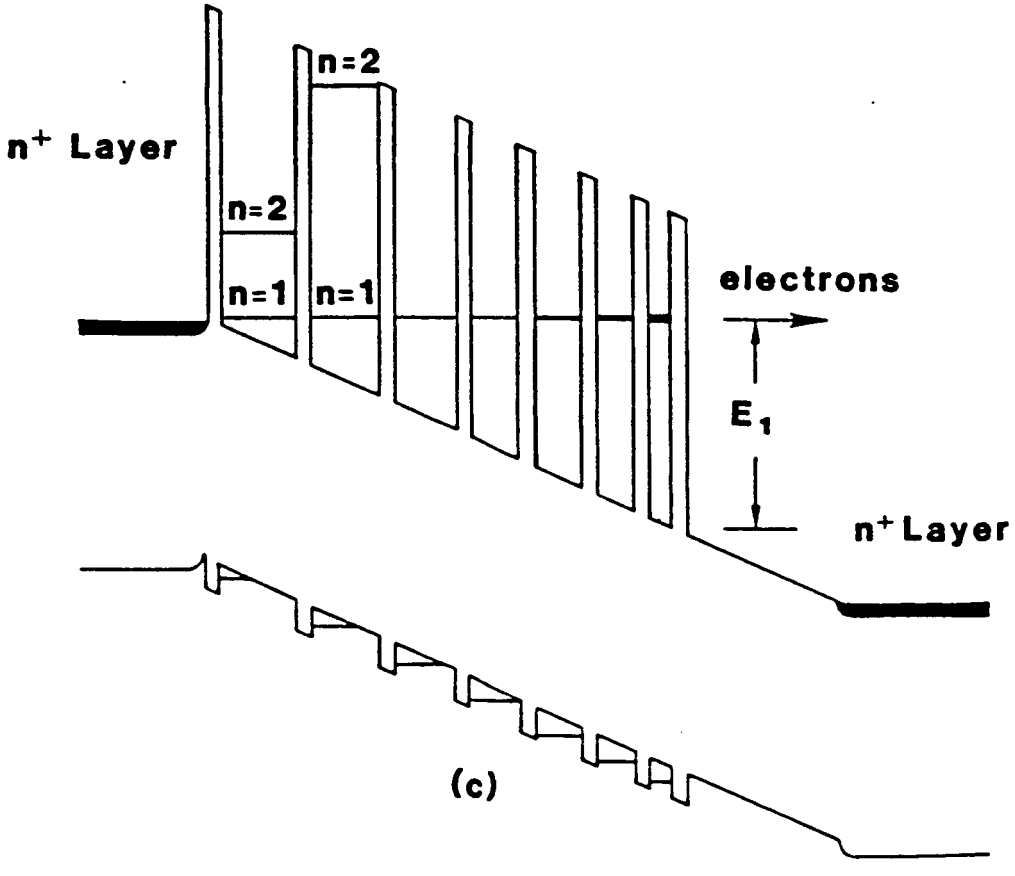

(c)

Fig 2
Brennan: Summers

Fig. 3
Brennan & Summers

ZnSe / $CaSrF_2$

10 Å Barriers, 2.5 Volts Bias

3 Wells	4 Barriers
28.0 Å	4.0 eV
6.8 Å	4.0 eV
6.5 Å	4.0 eV
	4.0 eV

M_{well} = 0.17

$M_{barrier}$ = 0.5

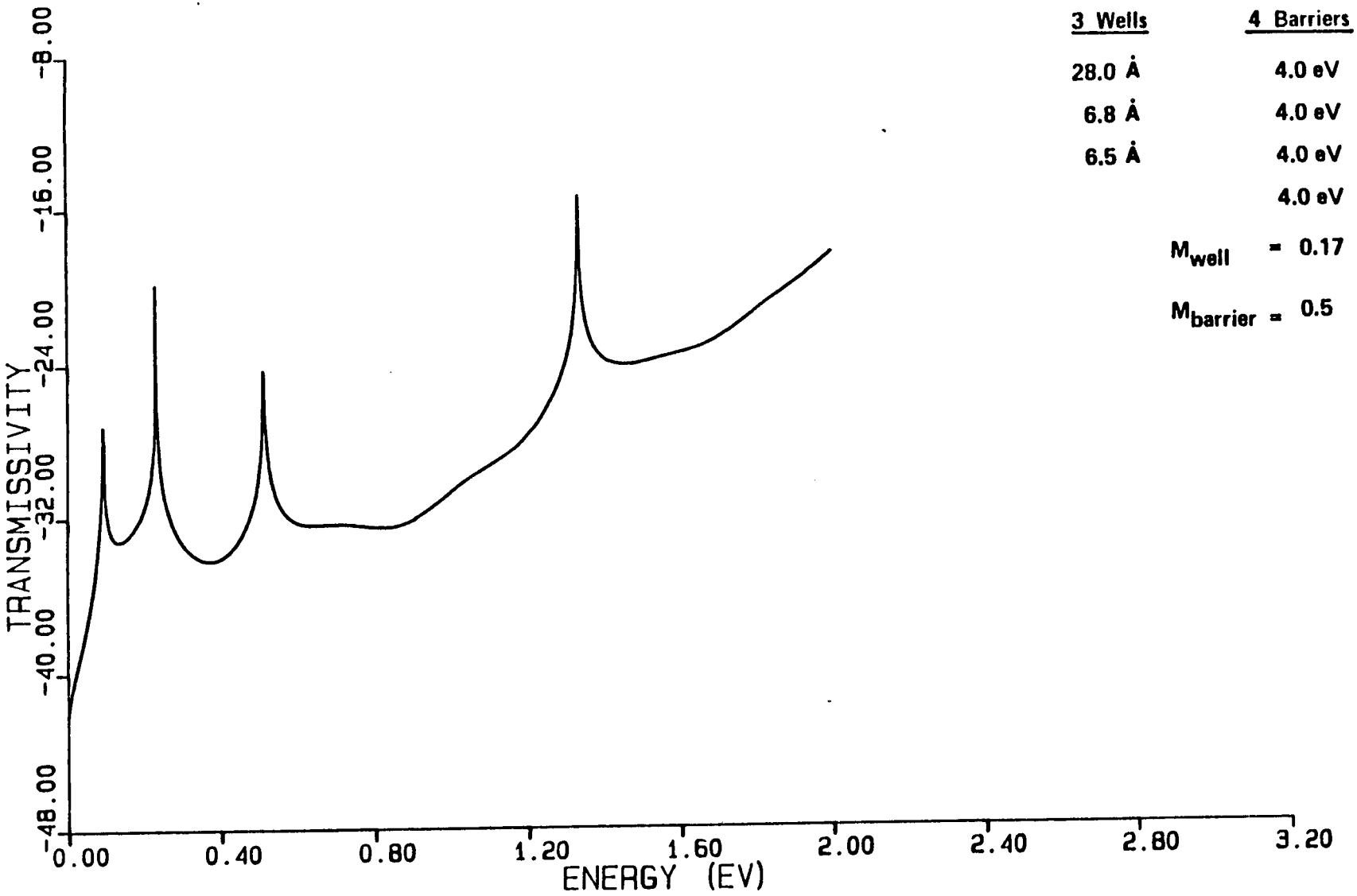

Fig. 4
Brennan: Summers

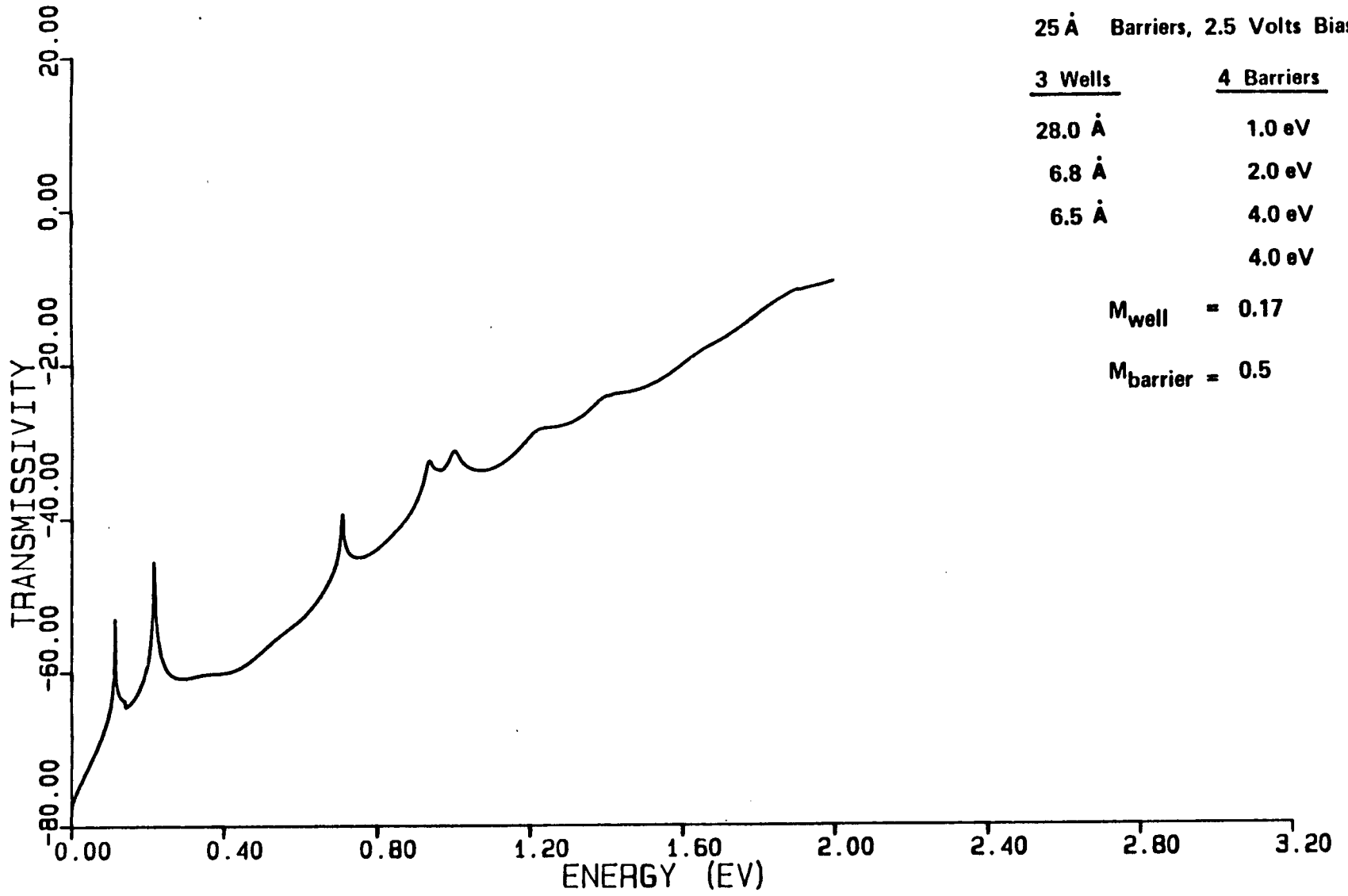

Fig. 5
Brennan: Summers

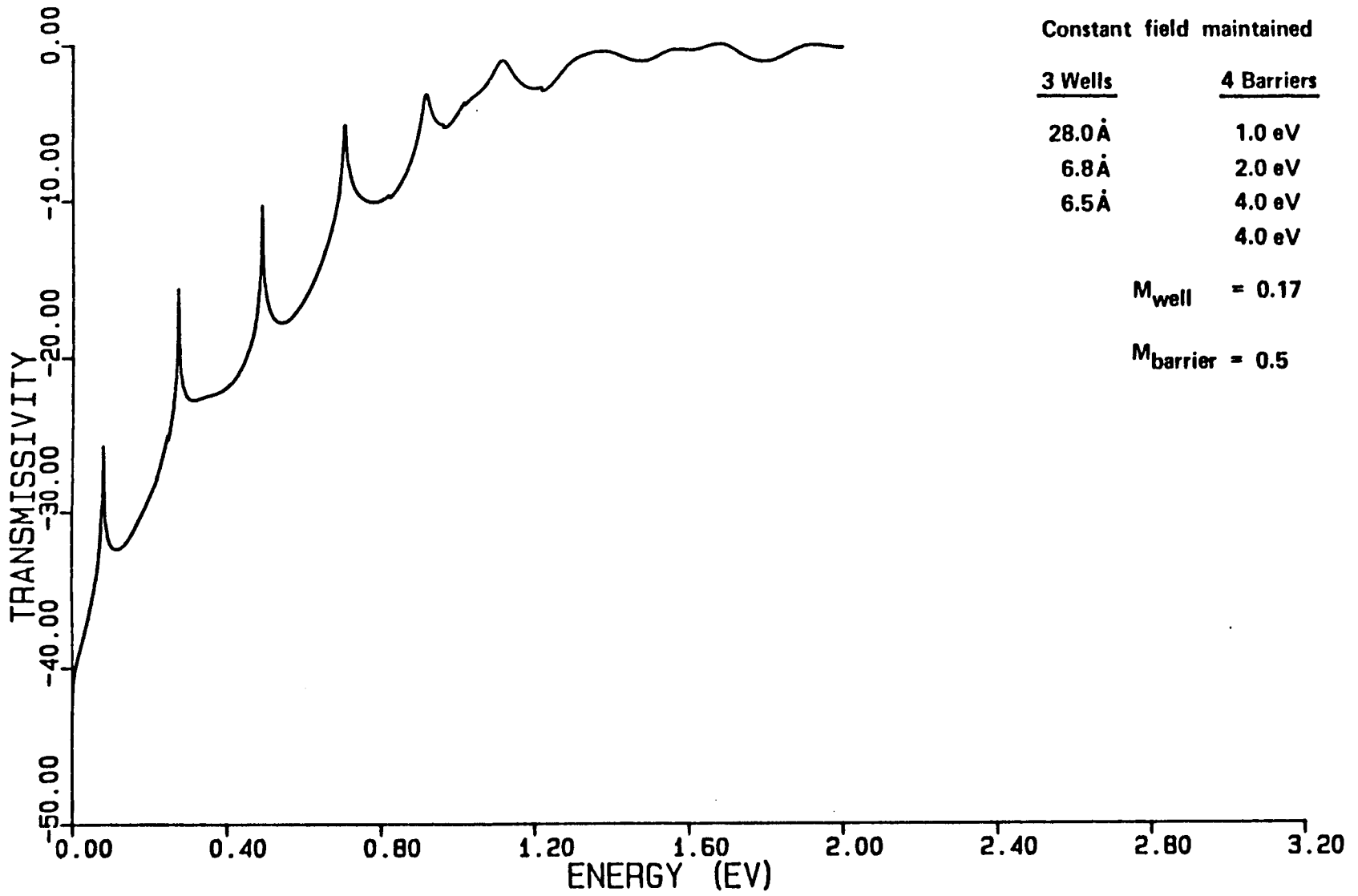

$ZnSe/CaSrF_2$

25 Å Barriers; 4.34 volts bias

Constant field maintained

3 Wells	4 Barriers
28.0 Å	1.0 eV
6.8 Å	2.0 eV
6.5 Å	4.0 eV
	4.0 eV

$M_{well} = 0.17$

$M_{barrier} = 0.5$

Fig. 6
Brennan Summary

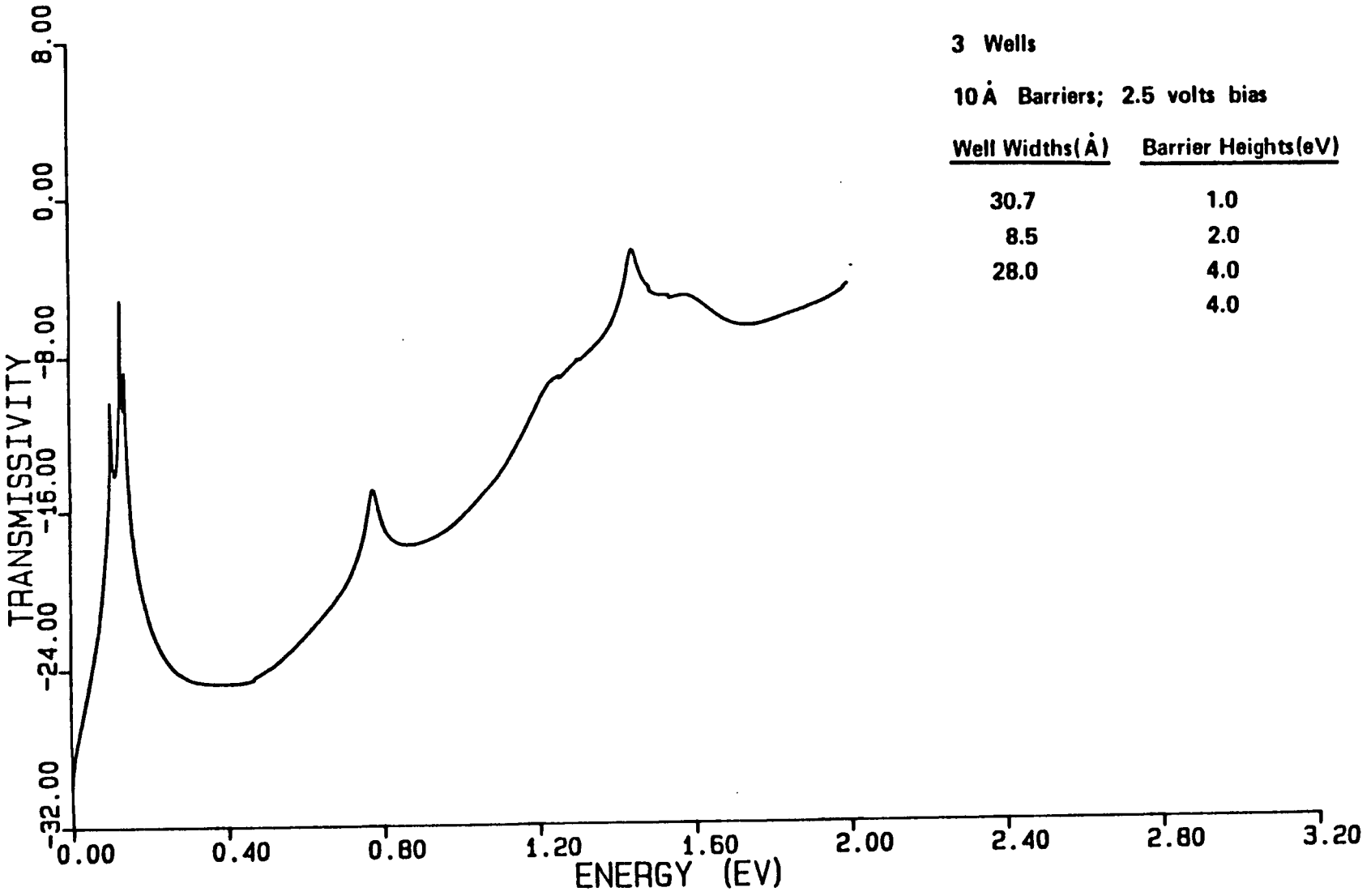

Fig. 7
Brennan: Summas

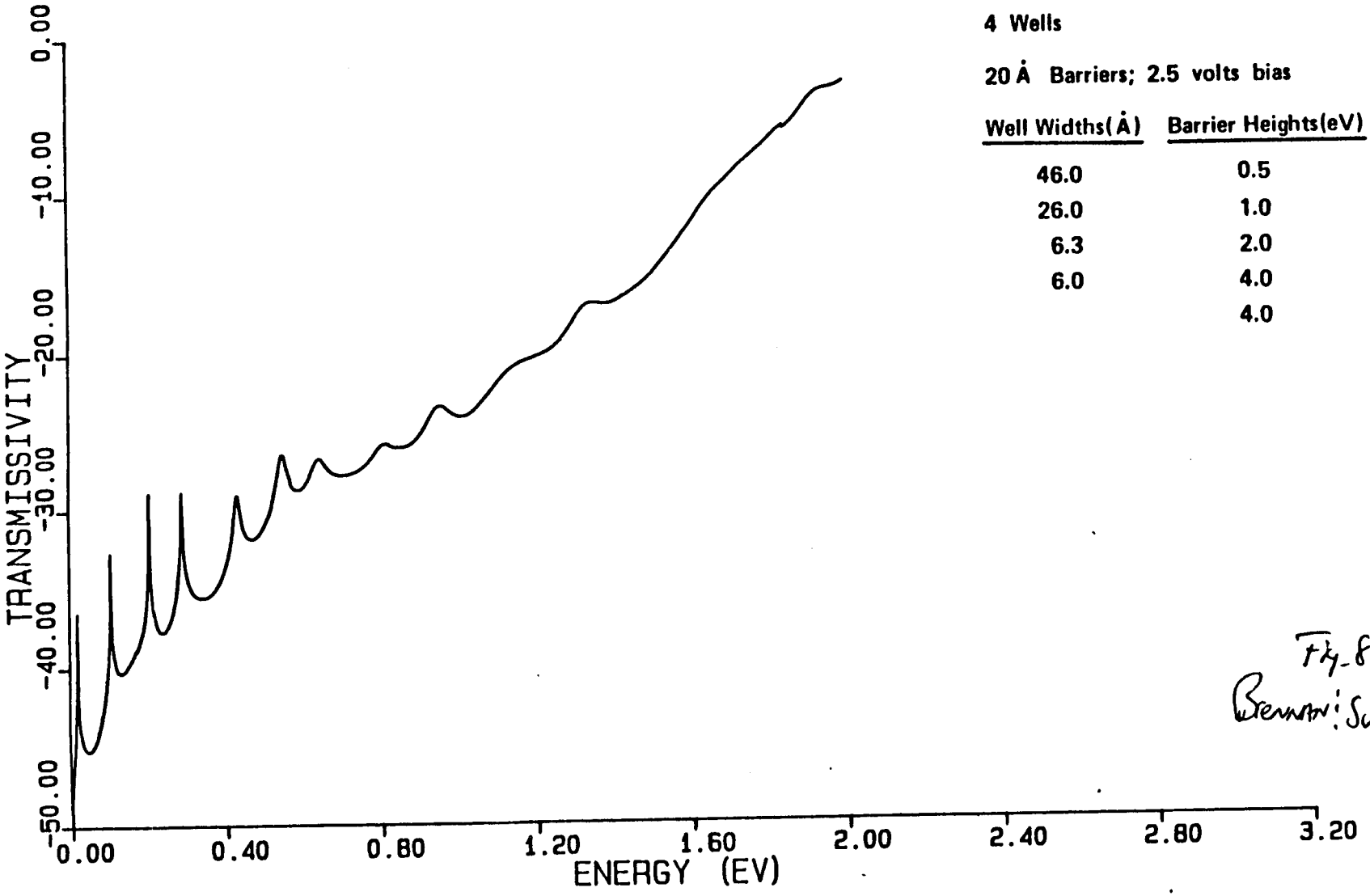

$ZnSe/CaSrF_2$

4 Wells

20 Å Barriers; 2.5 volts bias

Well Widths(Å)	Barrier Heights(eV)
46.0	0.5
26.0	1.0
6.3	2.0
6.0	4.0
	4.0

Fig. 8
Brennan & Summers

ZnSe

Injection Energy = 2.5 eV

Applied Field = 10kV/cm

Curve	Elapsed Time(psec)	Mean Dist.(Å)
1	0.1	108.5
2	0.2	199.0
3	0.3	244.0

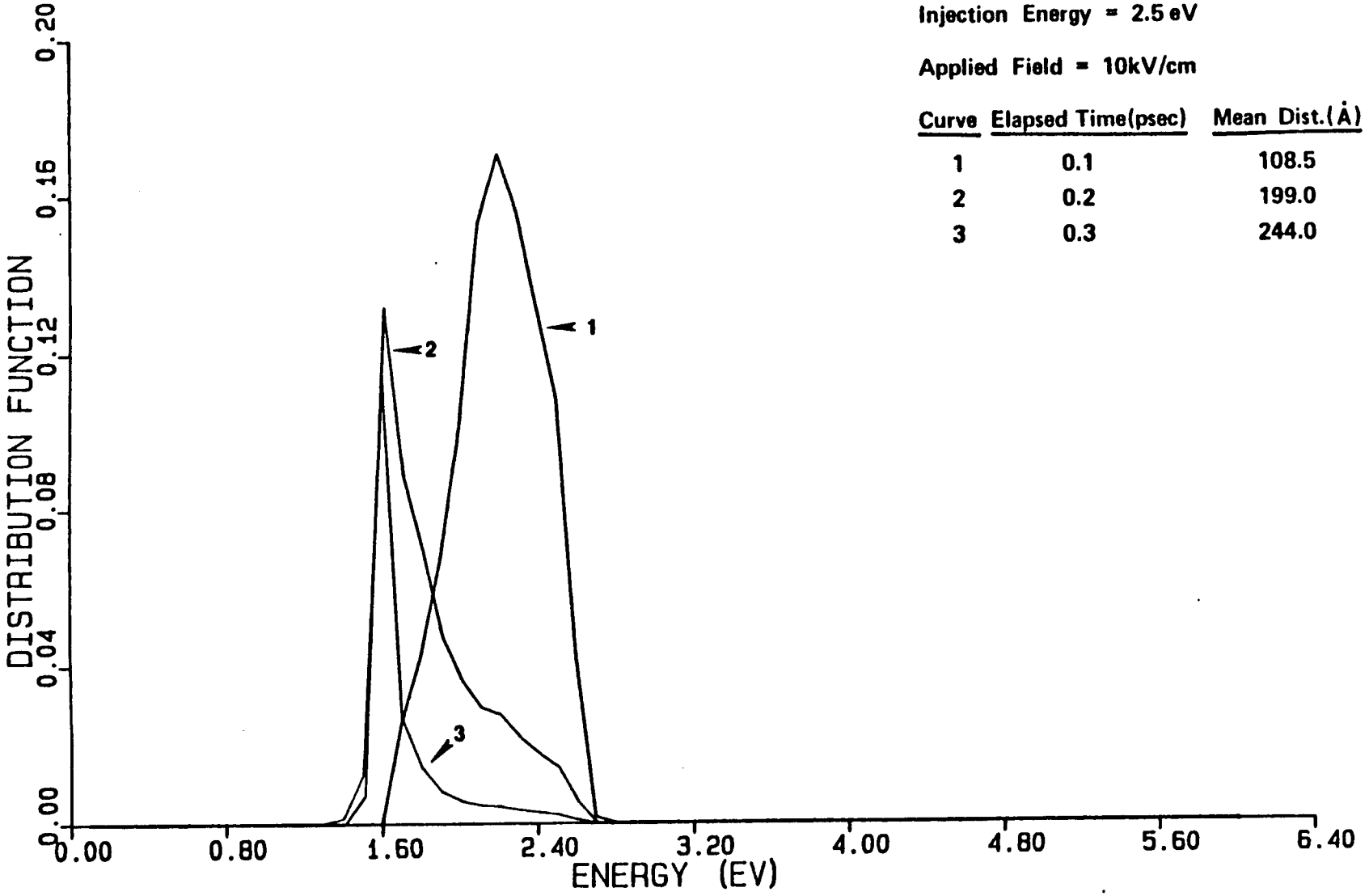

Fig. 9

Brennan/Summers

ZnSe 300K

Injection Energy = 2.5 eV

Applied Field = 30 kV/cm

Curve	Elapsed Time(psec)	Mean Dist. (Å)
1	0.1	140
2	0.2	185
3	0.3	260

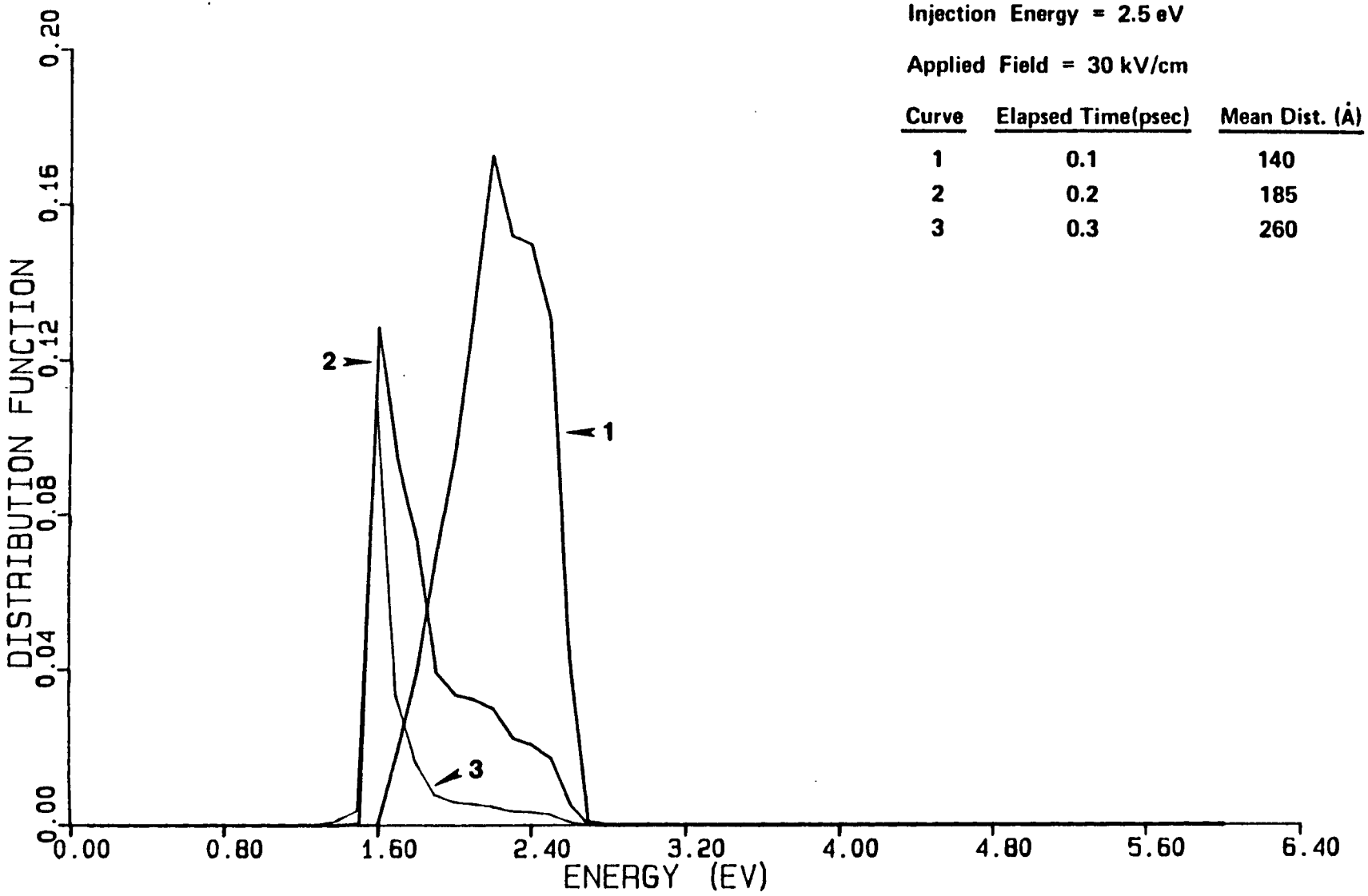

Fig. 10

Brennan: Summers

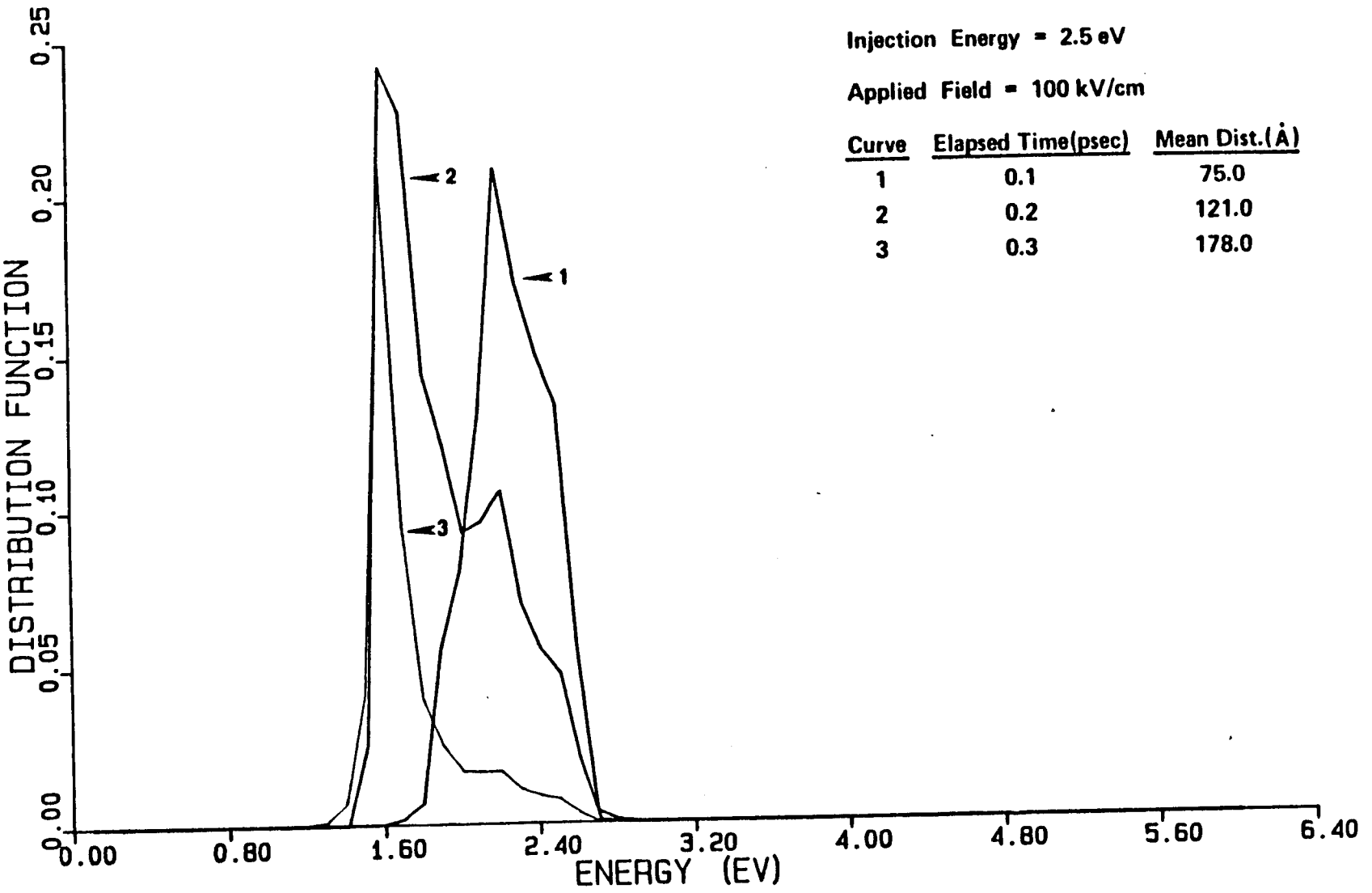

Fig. 11
Brennan: Summers

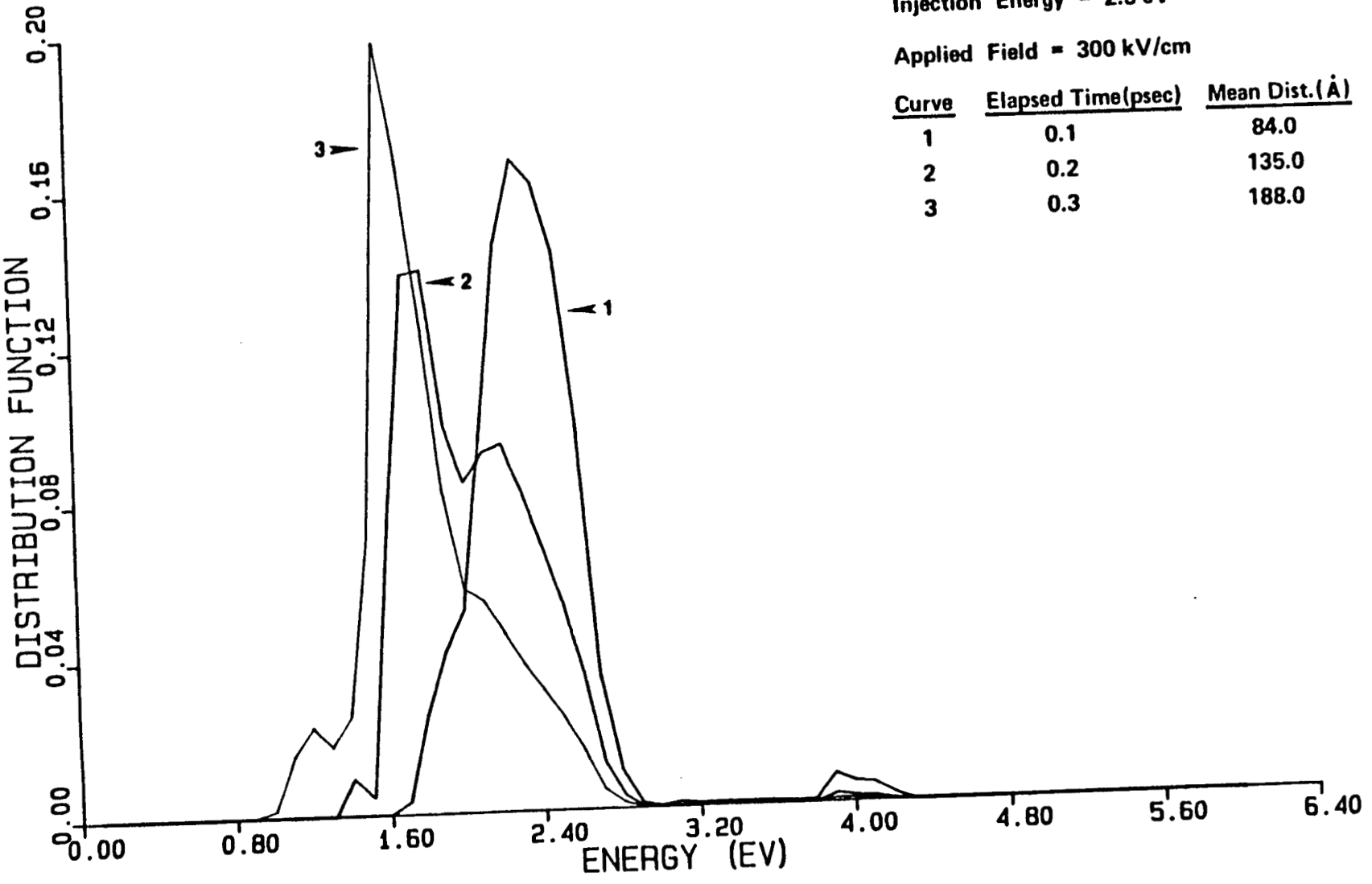

Fig. 12
Brennan; Summers

ZnSe

Injection Energy = 2.5 eV

Applied Field = 500 kV/cm

Curve	Elapsed Time(psec)	Mean Dist.(Å)
1	0.1	66.0
2	0.2	130.0
3	0.3	186.0

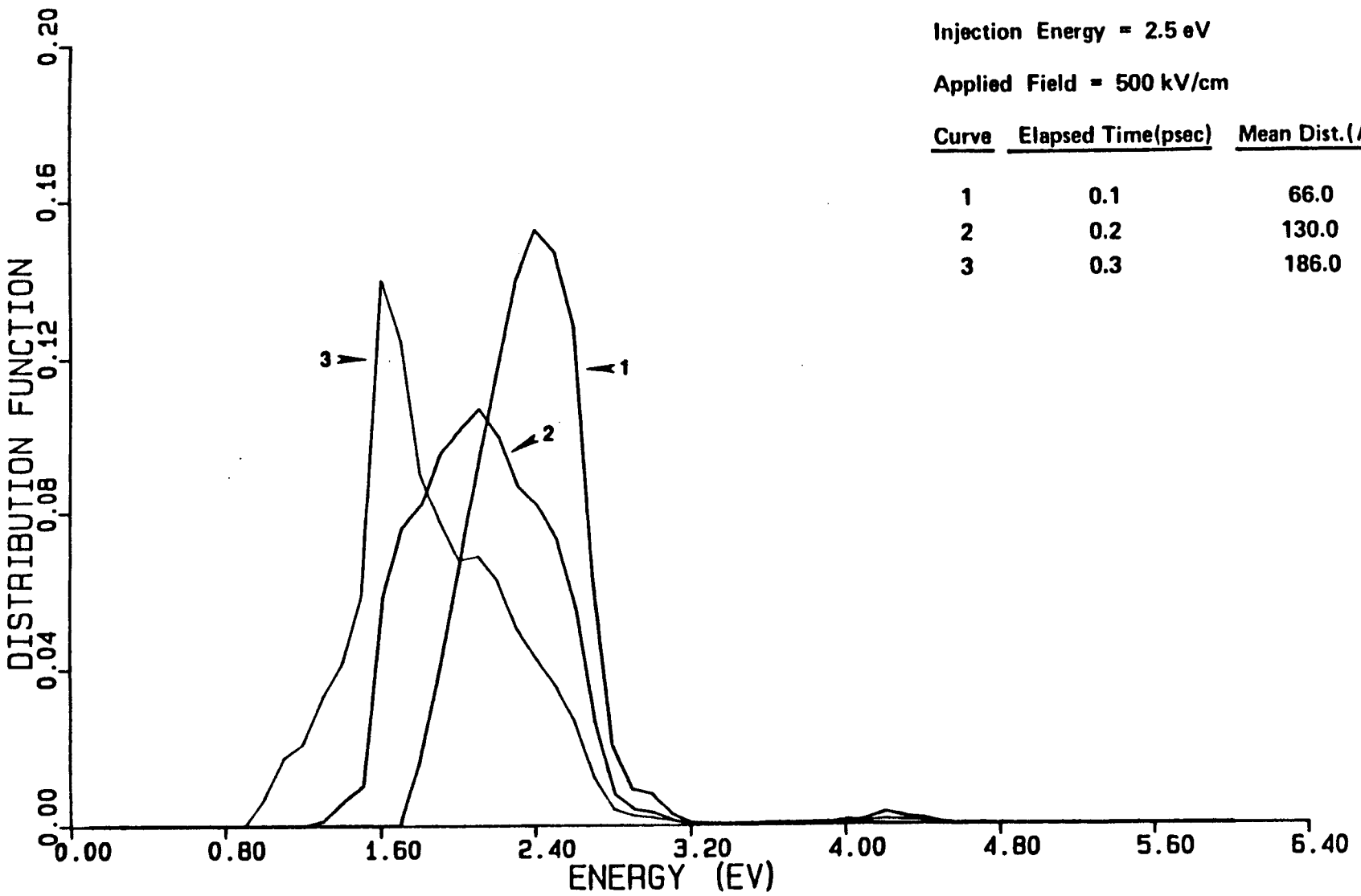

Fig. 13
Brennan: Summers

ZnSe

Injection Energy = 2.5 eV

Applied Field = 1000 kV/cm

Curve	Elapsed Time(psec)	Mean Dist. (Å)
1	0.1	80.0
2	0.2	144.0
3	0.3	197.2

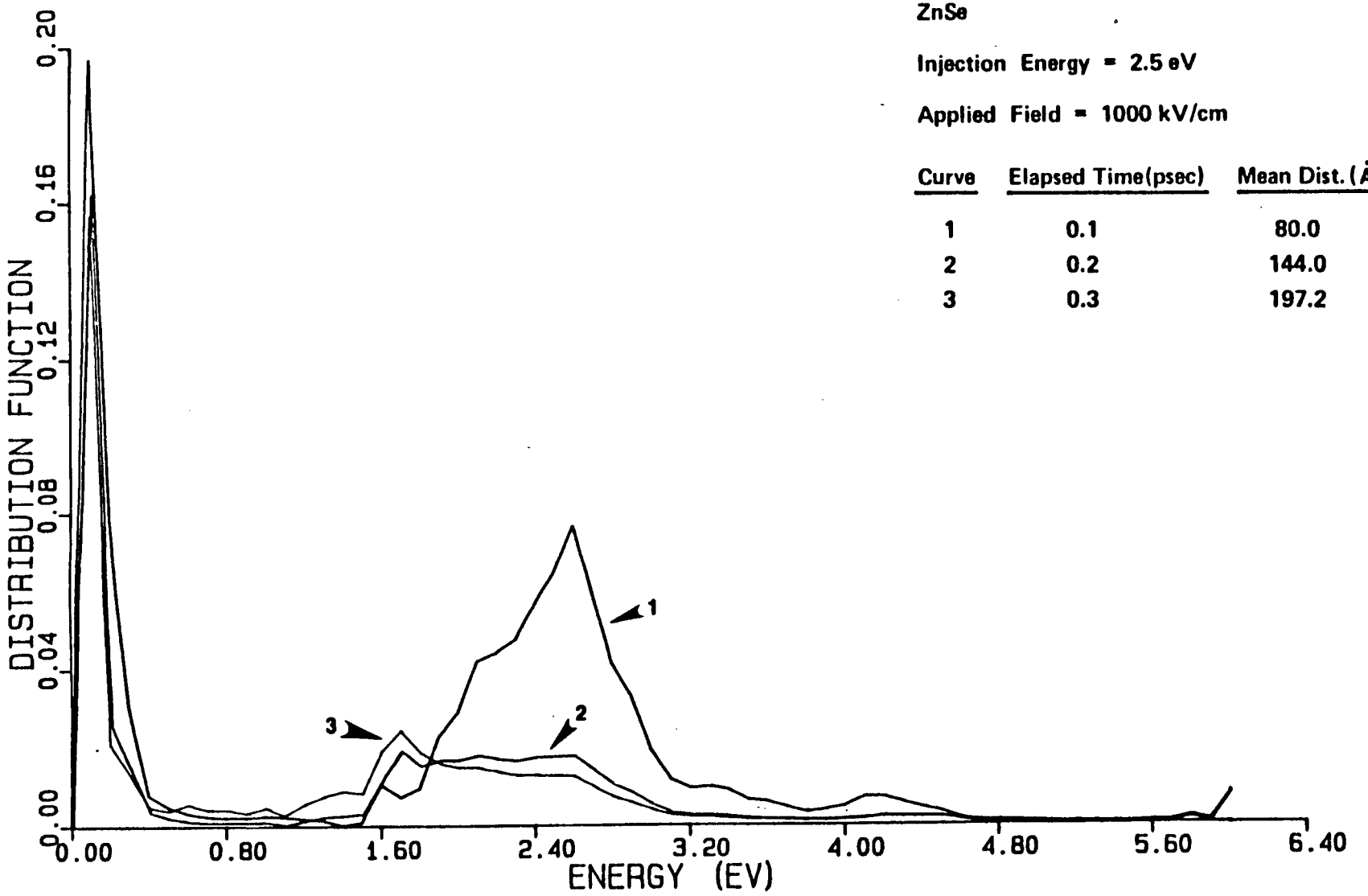

Fig. 14
Brennan: Summers

2. Heteroepitaxial Growth of ZnS by MBE

In the initial phase of research on heteroepitaxial ZnS films, different growth conditions were investigated to determine those optimum for ZnS growth on GaAs or Si substrates. The first goal was to obtain epitaxial films of uniform thickness and good surface morphology. The layers were studied principally by in-situ Reflection High Energy Electron Diffraction (RHEED) in order to understand the relationship between epitaxial film nucleation conditions and surface structure. Phase-contrast microscopy was used to determine surface roughness and step profilometry to measure film thickness.

The first choice of substrates for the heteroepitaxial growth of ZnS were (100)-oriented GaAs. GaAs was chosen because of previous experience at Georgia Tech with the growth of other II-VI compounds such as CdTe and ZnTe on this substrate. The growth of epitaxial ZnS on GaAs substrates has been demonstrated using both MBE and Organometallic Vapor Phase Epitaxy (OMVPE)[1-3], although little film characterization was reported and no results on Mn doping were presented.

2.1 Growth of ZnS on GaAs Substrates

Ten runs were made on (100)-oriented GaAs, with the growth conditions and film results summarized in Table 1. Runs #3-7 were performed in a MBE system designed and built at GTRI, and runs #8-10 in a commercial Varian MBE/Gen II system. The homemade MBE is equipped with separately-pumped load-lock, isolation chamber and growth chamber. Vacuum conditions before and during growth were recorded by a Quadrapole Mass Spectrometer (QMS). With the source furnaces at their operating temperatures and the LN_2-shrouds cooled the base pressure was at the X-Ray limit of the Bayard-Alpert gauge, $1x10^{-9}$torr. QMS indicated the residual gases were composed mostly of H_2 and CO with negligible amounts of H_2O and hydrocarbons. A typical QMS spectrum is shown in Fig. 1.

After chemical preparation and loading, the GaAs substrates were transferred to the isolation chamber until needed for growth. Before a growth run, the substrates were placed in the growth chamber and outgassed overnight at a temperature of 250°C-400°C to remove low vapor pressure

contaminants and allow the vacuum conditions to stabilize before epitaxy. Polycrystalline ZnS chunks from Raytheon and CVD, Inc. were used in a single graphite furnace to produce molecular beams of Zn and S_2.

Growth runs #3-6 yielded poor films or no films at all. The results stemmed from two possible causes. First, the beam-equivalent pressures (BEP) of Zn and S_2 were too small to nucleate a film due to evaporation of the Zn and/or S_2 atoms from the substrate. This effect is substantiated by the experimentally observed small sticking coefficients of Zn and S_2 on the GaAs surface[4]. Secondly, our chemical cleaning and mounting procedure for these four GaAs substrates did not produce a sufficiently thick surface oxide to prevent surface degradation (i.e. Arsenic loss) during substrate outgassing. Also, it is possible that the oxide on the GaAs was not completely desorbed before growth. Therefore, for the next set of substrates an improved wet chemical cleaning procedure was used. These substrates were also air-baked at 300°C in dust-free conditions to form a uniform, protective surface oxide layer. The first growth run using these substrates, #7, was quite encouraging. The oxide desorption temperature was accurately determined using the RHEED pattern as 690°C, as shown in Fig. 2. A RHEED pattern of the growing film is shown in Fig. 3. Although the pattern is spotty and indicates three-dimensional growth and surface roughness on a sub-micron scale, no extra diffraction spots due to film twinning are visible. Also, Kikuchi band formation was observed toward the end of film growth indicating improving crystalline quality. Phase-contrast microscopy showed a smooth, featureless surface at 1000x magnification for Run #7.

The next ZnS growth runs, #8-10, on (100)-oriented GaAs were performed in a Varian MBE/Gen II dedicated to II-VI materials. A PBN crucible loaded with CVD, Inc. ZnS was used to produce the molecular beams of Zn and S_2. Substrates were chemically cleaned using the procedure of Growth Run #7 and placed in the load lock where they were outgassed at 400°C for approximately 4 hrs at 10^{-6} torr. After cooling the LN_2-shrouds and bring the ZnS oven to its deposition temperature, the GaAs substrates were loaded into the growth chamber and heated to 500°C to further outgas the substrate. During this step the substrate was turned away from the source flange to minimize contamination of the growth position.

After observing the oxide desorption from the GaAs surface with RHEED, the shutter to the ZnS furnace was opened to allow a Zn and S_2 flux to be incident on the GaAs surface while at the oxide desorption temperature. Previous ZnS/GaAs runs did not have Zn and S_2 fluxes incident on the GaAs until the substrate temperature had dropped by approximately 300°C. The RHEED pattern after oxide desorption showed a Ga-rich surface. With Zn and S_2 fluxes incident, the GaAs surface smooths and reconstructs as shown in Fig. 4. The change in the surface reconstruction is hypothesized to result from the formation of a surface GaAs:S layer, in analogy to similar reaction observed between the GaAs surface and elemental Se and Te [5-7]. There is a possibility that through control of the composition of this surface layer, improved lattice matching or decreased epitaxial layer strain may be achieved. Research is underway to better understand this surface layer and optimize it for improved epitaxial layer quality. It should be noted however, that at this high substrate temperature no film grows on the GaAs surface.

As the substrate temperature was lowered from the oxide desorption temperature under the Zn and S_2 fluxes, the reconstruction of Fig. 4 was lost, although the RHEED pattern remained streaky. For further decrease in substrate temperature, the RHEED pattern becomes spotty as shown in Fig. 5. This change was attributed to the beginning of ZnS growth, although no film was observed until the substrate temperature dropped another 200°C to 250°C-185°C. At this temperature a uniform, colored film was visible on the substrate. With continued growth there is a drastic improvement in the RHEED pattern, with 2-fold reconstruction and bright Kikuchi band formation as shown in Fig. 6. Analysis of the RHEED patterns shows that the ZnS layer grows with a (100) surface orientation aligned with the (100)-oriented GaAs substrate. Examination of these epitaxial layers with phase-contrast microscopy showed a smooth surface except for small defects due to particulate contamination on the surface. However, SEM imaging of the surface at a glancing angle revealed a slight surface texture not revealed by phase-contrast microscopy. Phase-contrast microscopy and SEM photographs of the ZnS/GaAs (100) Growth Run #8 surface are shown in Figs. 7 and 8, respectively.

The RHEED patterns and surface morphology results for growth runs #8-10 were the best for any layer grown on either GaAs or Si substrates.

In fact, a comparison of RHEED patterns for heteroepitaxial ZnS from the literature and from runs #8-10 shows the latter to be far superior in terms of intensity and uniformity of the streaked pattern and the brightness of the Kikuchi bands[1,8-13]. Presently a set of growth runs is under way to optimize ZnS quality as assessed by double crystal rocking curves (DCRC). Through DCRC the concentration of point defects, dislocations and the epitaxial layer strain can be determined and minimized to give layers capable of high luminescence intensity when doped with Mn.

2.2 Growth of ZnS on Si Substrates

The other choice of substrate for heteroepitaxial growth of ZnS was Si. The principal problem associated with the use of GaAs as a substrate for ZnS epitaxial growth is the large lattice mismatch between ZnS and GaAs (approx. 3.7%) which can produces a high density of misfit and threading dislocations in the ZnS epitaxial layer. Problems also exist because of the outdiffusion of Ga and As into the ZnS layer, resulting in compensating doping of the film. This effect is observed in heteroepitaxial ZnSe layers on GaAs[14,15]. In contrast, Si and ZnS are lattice-match to better than 0.2% at room temperature, and Si diffusion into the ZnS layer from the Si substrate should be negligible due to better lattice matching and the lower reactivity of Si. Other advantages of Si substrates are their high crystalline quality, superior surface finish, mechanical strength and availability in large surface areas at comparatively low cost. From a more device-oriented comparison, Si is an ideal substrate for performing the x-y biasing and logic addressing in a composite ZnS/Si EL display panel.

The major difficulty associated with heteroepitaxial or homoepitaxial layers on Si was attributed to the surface preparation [3,11,16]. Ideally, the Si surface must have a thin, porous, chemically grown surface oxide to protect it from atmospheric carbon contamination (which inhibits epitaxial nucleation), but which can be desorbed at temperatures less than 900°C to avoid thermal defect formation. Recently, Ishizaka, et al.[16] published a chemical treatment used for the epitaxial growth of both GaAs and Si on Si substrates. This cleaning procedure is given in Table 2 and produces a reproducible surface oxide. This cleaning procedure was used on (111)-oriented Si since it was reported that surface oxides on (111)-oriented Si

decompose at 100°C less than oxide layers on (100)-Si surface[16].

The ZnS growth runs on Si were performed in the Varian MBE/GenII machine used for the last three ZnS growth runs on GaAs. After chemical treatment and In-mounting, the Si substrates were loaded into the load lock and outgassed at 600°C for 3-4 hours. The substrates were kept under a vacuum of $4x10^{-9}$torr until their use in a growth run. Background pressure during growth was approximately $1x10^{-9}$torr, although pressures were almost two orders of magnitude higher during the Si surface oxide desorption step because of the high temperature of the substrate and manipulator. The growth conditions and film results for ZnS on (111)-oriented Si are shown in Table 3. Based on these results, a tentative model has been formulated for growth. After oxide desorption, the Si substrate has the literature-reported (7x7) surface reconstruction shown in Fig. 9. A variety of surface reconstructions appeared as the substrate temperature was decreased from the oxide desorption temperature to the growth temperature. When a flux of Zn and S_2 was incident on the substrate above 300°C, the surface reconstruction changed to a (2x2) pattern as shown in Fig. 10. Note that the pattern shows little (no) intensity modulation along the zero-order Laue zone and exhibits well defined higher order Laue zones. Such features result from the long-range periodicity and high crystalline quality of the Si substrate and surface. However, no observable ZnS deposition occurred on the Si substrate under these conditions, although the (2x2)-reconstruction pattern was clearly associated with the Zn- and S_2-fluxes. The absence of film growth coupled with the surface reconstruction dependence on incident flux at substrate temperatures above 300°C suggests that either Zn or S, but not both, resides on the (111)-Si surface with some steady-state coverage. Future work using Auger Election Spectroscopy (AES) or X-Ray Photoelectron Spectroscopy (XPS) is planned to determine the chemical composition of the (2x2)-reconstructed Si surface.

At substrate temperatures below 300°C, the substrate begins to color, indicating ZnS film growth. Therefore, the sticking coefficient of either the Zn or S (which ever component is not responsible for the (2x2) surface reconstruction) must be large enough to nucleate the film. However, the surface morphology and crystalline quality of these layers, as assessed by RHEED, was poor. A possible cause was non-optimum nucleation conditions for these films. Considering the small surface mobilities at substrate

temperatures below 300°C, improved surface quality and growth conditions are needed to insure defect-free nucleation of the epitaxial layers. A more obvious problem was the In loss that was observed to occur during oxide desorption. Because the Si substrates are attached to molybdenum blocks with liquid In, at the temperatures needed to desorb the surface oxide (approx. 800°C-900°C) significant amounts of In evaporate from underneath the substrate. This loss of thermal contact results in large temperature gradients across the substrate, incomplete surface oxide desorption and the possibility of the substrate falling off! The two former problems are believed to be the cause of the nonuniformities observed in the thickness of the ZnS epitaxial films.

As a result of these studies we are presently concentrating our growth activities on the use of GaAs substrates and expect to present a paper on this work at the Third International Conference on II-VI Compounds.

In conjunction with these growth studies we are making preparations to do In-free mounting for one- or two-inch Si wafers and also investigating the potential of photo-assisted MBE growth and/or chemical beam epitaxy of ZnS. Both of these growth techniques were recently reported in the literature and have demonstrated II-VI films of improved crystalline perfection and controllable doping.

References

1. K. Yoneda, T. Toda, Y. Hishida and T. Niina, J. Crystal Growth, 67(1984) 125-134.

2. S. Fujita, Y. Tomamura and A. Sasaki, Jpn. J. Appl. Phys. 22(1983) L583-L585.

3. P.J. Wright, R.J.M. Griffiths and B. Cockayne, J. Crystal Growth 66(1984) 26-34.

4. M. Naganuma and K. Takahashi, Phys. Status Solid (a)31(1975) 187.

5. D.W. Tu and A. Kahn, J. Vac. Sci. Technol. A3(1985) 922-925.

6. R.D. Feldman, R.F. Austin, D.W. Kisker, K.S. Jeffers and P.M. Bridenbough, Appl. Phys. Lett. 48(1986) 248-250.

7. R.D. Feldman and R.F. Austin, Appl. Phys. Lett. 49(1986) 954-956.

8. M. Yokoyama and S. Ohta, J. Appl. Phys. 59(1986) 3919-3921.

9. M. Yokoyama, K. Kashiro and S. Ohta, Appl. Phys. Lett. 49(1986) 411-412.

10. M. Yokoyama, K. Kashiro and S. Ohta, J. Appl Phys. 60(1986) 3508-3511.

11. K. Hirabayashi and O. Kogure, Jpn. J. Appl. Phys. 24(1985) 1590-1593.

12. T. Yao and S. Maekawa, J. Crystal Growth 53(1981) 423-431.

13. T. Matsumoto and T. Ishida, J. Crystal Growth 67(1984) 135-140.

14. H.A. Mar and R.M. Park, J. Appl. Phys. 60(1986) 1229-1232.

15. T. Yao, M. Ogura, S. Matsuoka and T. Morishita, Appl. Phys. Lett. 43 (1983) 499-501.

16. A. Ishizaka and Y. Shiraki, J. Electrochem. Soc. 133(1986) 666.

17. M. Akiyama, Y. Kawarada and K. Kaminishi, Jpn. J. Appl. Phys. 23(1984) L843-L845.

18. R.C. Pond, P.P. Gowers, D.B. Holt, B.A. Joyce, J.H. Neave and P.K. Larsen, Mat. Res. Soc. Symp. Proc. 25(1984) 273-278.

LIST OF TABLES

Run	Maximum Substrate Temp.	Growth Temp.	Beam Equivalent Pressure	Time of Growth	Film
#3	630°C	300°C	1.8×10^{-7} torr	5 hrs, 32 min	No film on substrate
#4	650°C	400°C	8.5×10^{-7} torr	2 hrs, 44 min	No film on substrate
#5	400°C	350°	8.4×10^{-7} torr	5 hrs	Nonuniform, purple film on substrate RHEED pattern shows twinning
#6	325°C	325°C	8.7×10^{-7} torr	4 hrs, 4 min	Same as Run #5, but green in color
#7	690°C	475°C	3.2×10^{-6} torr	4 hrs, 40 min	Uniform, gold film on substrate; smooth surface morphology
#8	700°C	180°C	4.4×10^{-7} torr	3 hrs, 16 min	Uniform, green film on substrate; smooth surface morphology
#9	600°C	250°C	2.1×10^{-8} torr	3 hrs, 3 min	No film on substrate ZnS furnace empty
#10	610°C	250°C	3.7×10^{-6} torr	2 hrs, 18 min	Uniform, purple film on substrate; smooth surface morphology

Table 1. Summary of results for heteroepitaxial ZnS on (100)-oriented GaAs.

1. Degreasing

Rinse in overflowing deionized water for 10 min.
Rinse twice in methyl alcohol bath for 5 min. with agitation
Boil in trichlorethylene bath for 15 min.
Rinse twice in methyl alcohol bath for 5 min. with agitation
Rinse in overflowing deionized water for 10 min.

2. HNO_3 boiling

Boil in HNO_3 bath at 130°C for 10 min. to etch Si surface region and to form the oxide layer.
Dip in 2.5% HF solution for 10-15s, to remove oxide.
Rinse in overflowing deionized water.
Check the surface. If the surface does not dry uniformly, the HNO_3 boiling procedure is done once again. Generally, 3-4 repetitions are performed.

3. NH_4OH boiling (alkali treatment)

Boil in a solution of $NH_4OH:H_2O_2:H_2O$ (1:1:3) at 90°C for 10 min to make a thin surface oxide.
(Mix NH_4OH and H_2O and bring to temperature. Just prior to use, add H_2O_2.)
Dip in 2.5% HF solution for 10-15s, to remove the oxide layer.
Rinse in overflowing deionized water.

4. HCl boiling (acid treatment)

Boil in a solution of $HCl:H_2O_2:H_2O$(3:1:1) at 90°C for 10 min. to make a thin surface oxide.
(Mix HCl and H2O and bring to temperature. Just prior to use, add H_2O_2.)
Rinse in overflowing deionized water for 10 min.
Check that the surface uniformly becomes wet.
Spin dry.

Chemicals used in this work were not specifically purified but commercial reagents were guaranteed as:

HNO_3: 64-66 w/o assay with less than 2ppm impurities;
HCl: 35-37 w/o assay with less than 7 ppm impurities;
H_2O_2: 30 w/o assay with less than 40 ppm impurities;
HN_4OH: 28-30 w/o assay with less than 10 ppm impurities;
HF (50%), methyl alcohol and trichlorethylene: semiconductor grade, deionized water: 14-15 M. ohm cm. alcohol.

Table 2. Ishizaka surface preparation for Si substrates from Reference 16.

Run	Maximum Substrate Temp.	Oxide Desorb?	Growth Temp.	Beam Equivalent Pressure	Time of Growth	Film
#1	970°C	No	970°C	3.4×10^{-6} torr	?	Nonuniform, polycrystalline film
#2	970°C	Yes	600°C-350°C	2.8×10^{-6} torr	3 hrs, 16 min	Nonuniform, colored film
#3	970°C	Yes	450°C	1.8×10^{-6} torr	3 hrs, 51 min	No film on substrate
#4	850°C	Yes	350°C	1.4×10^{-6} torr	?	Polycrystalline film
#5	900°C	Yes	450°C-250°C	4.1×10^{-6} torr	4 hrs, 17 min	Polycrystalline/twinned film
#6	970°C	Yes(?)	450°C-250°C	5.8×10^{-7} torr	5 hrs, 21 min	Single crystal film, green in color
#7	970°C	No	900°C-275°C	1.1×10^{-6} torr	6 hrs, 8 min	Single crystal/twinned film, brown in color

Table 3. Summary of results for heteroepitaxial ZnS on (111)-oriented Si.

LIST OF FIGURES

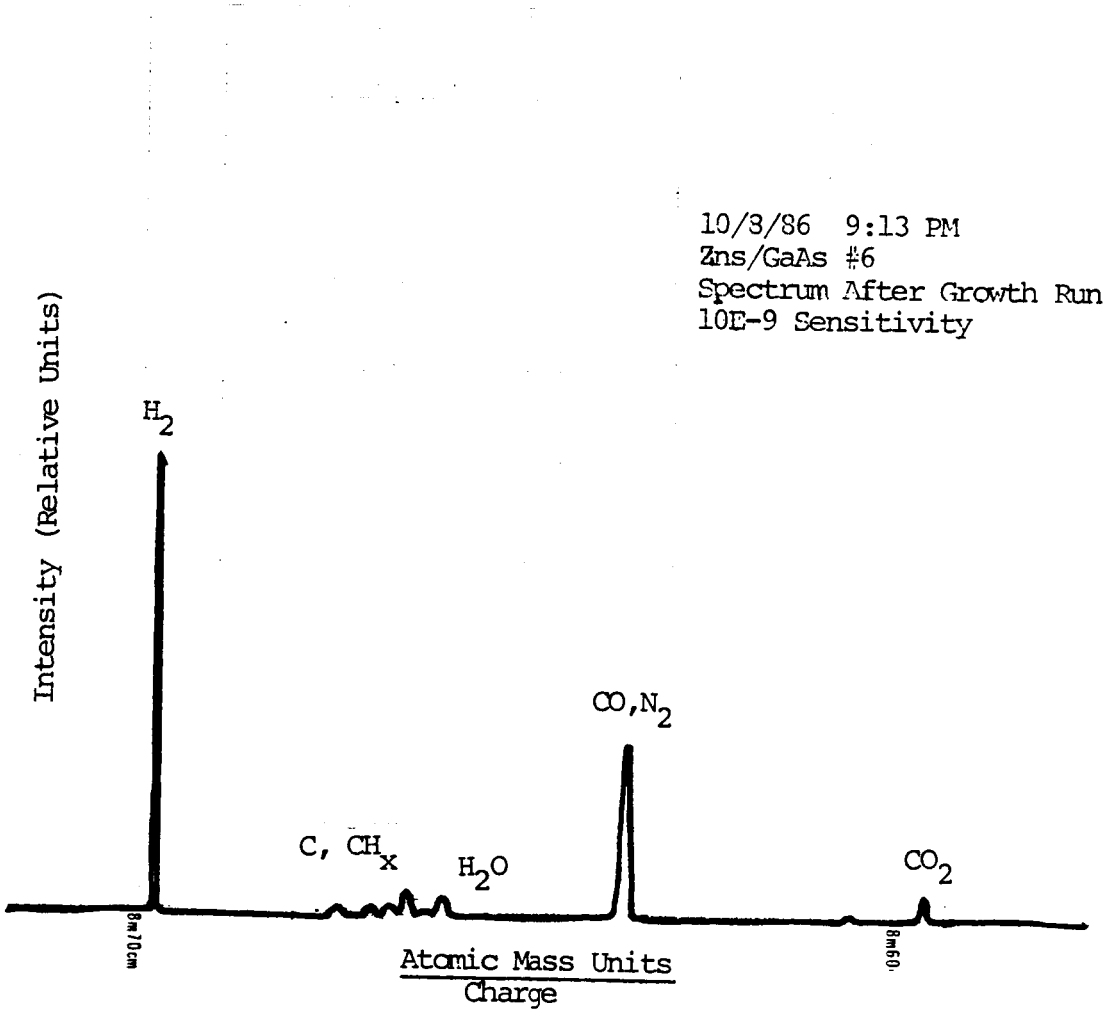

Figure 1. QMS spectrum for ZnS/GaAs #6.

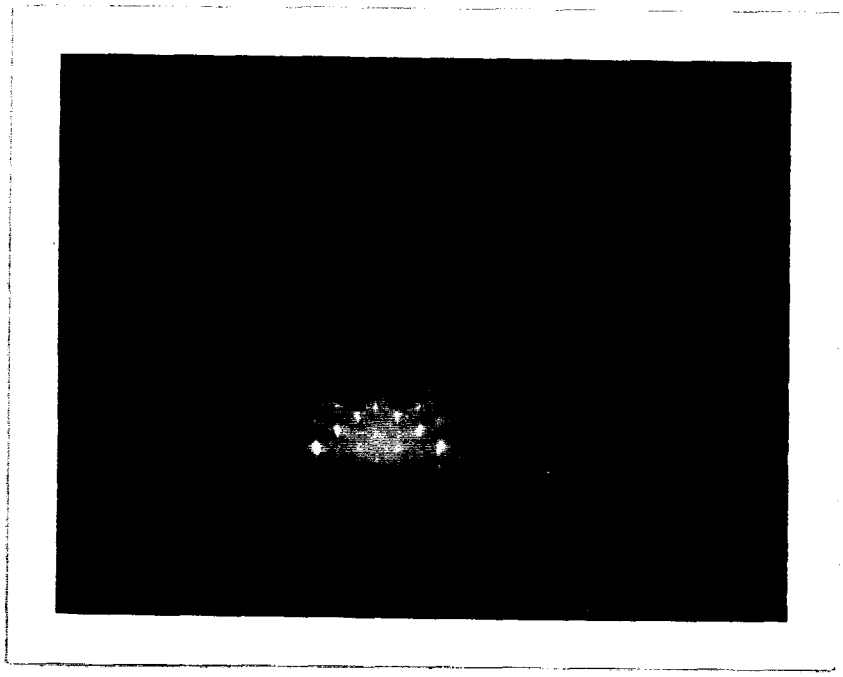

Figure 2. RHEED pattern of (100)-GaAs surface after oxide desorption.

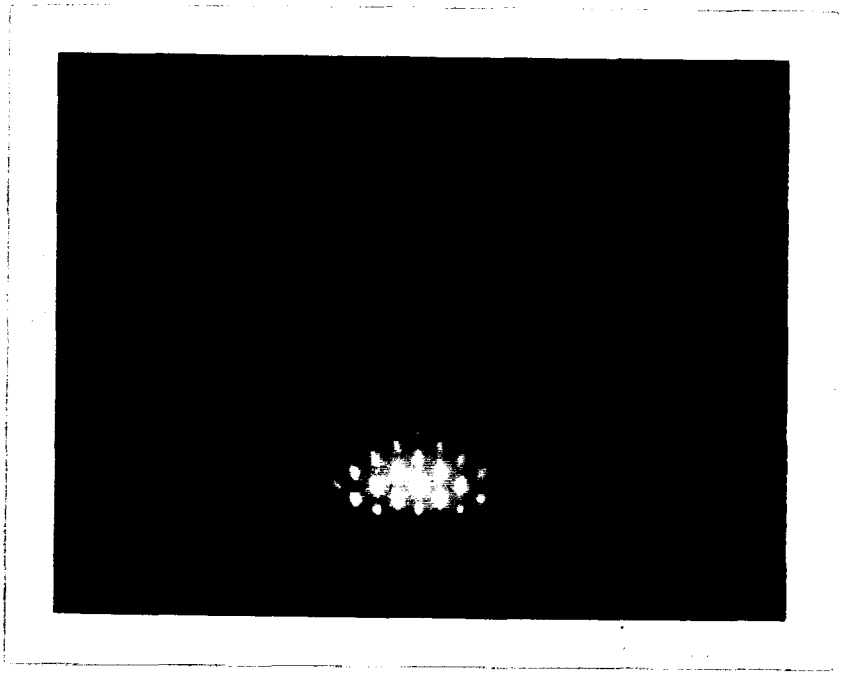

Figure 3. RHEED pattern of heteroepitaxial ZnS layer on (100)-GaAs.

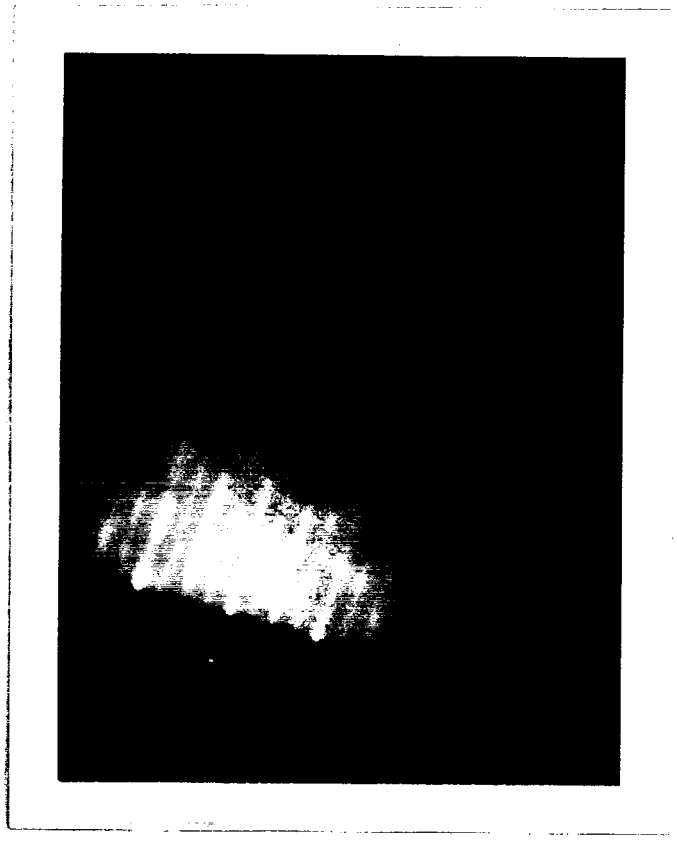

Figure 4. RHEED pattern of (100)-GaAs surface with S_2 and Zn fluxes incident at elevated temperatures.

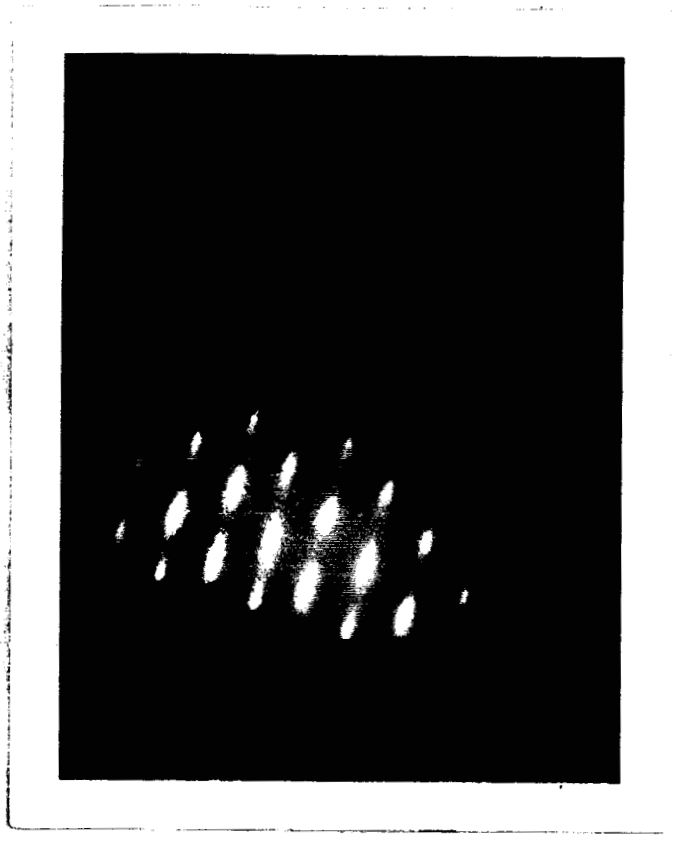

Figure 5. RHEED pattern of (100)-GaAs surface with S_2 and Zn fluxes incident as substrate temperature is lowered.

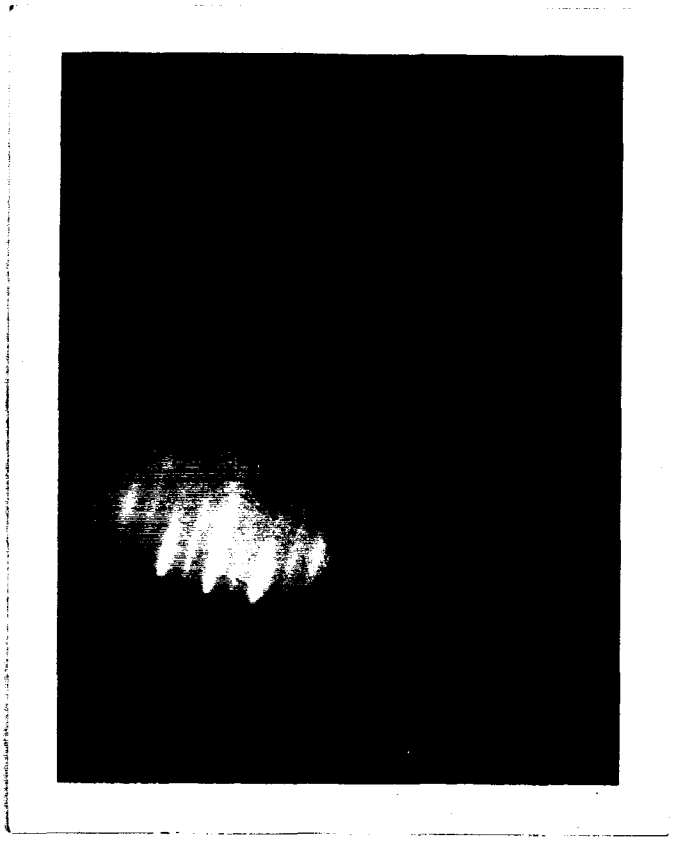

Figure 6. RHEED pattern of (100)-ZnS epitaxial layer on (100)-GaAs substrate.

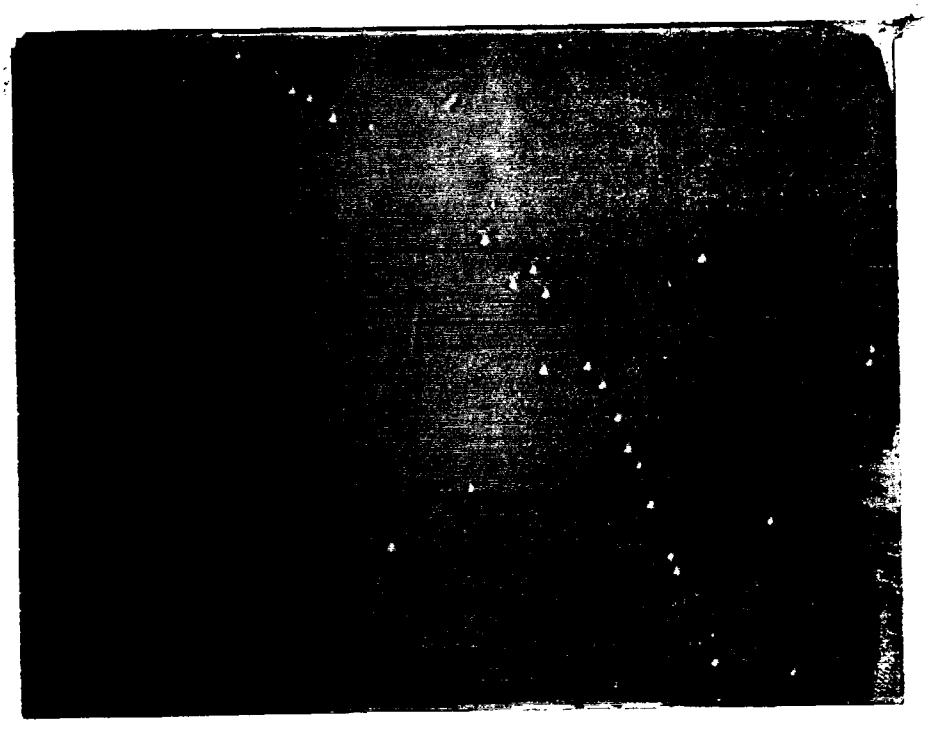

Figure 7. Phase-contract microscopy photograph of ZnS surface from Growth Run #8. Magnification is 1000X.

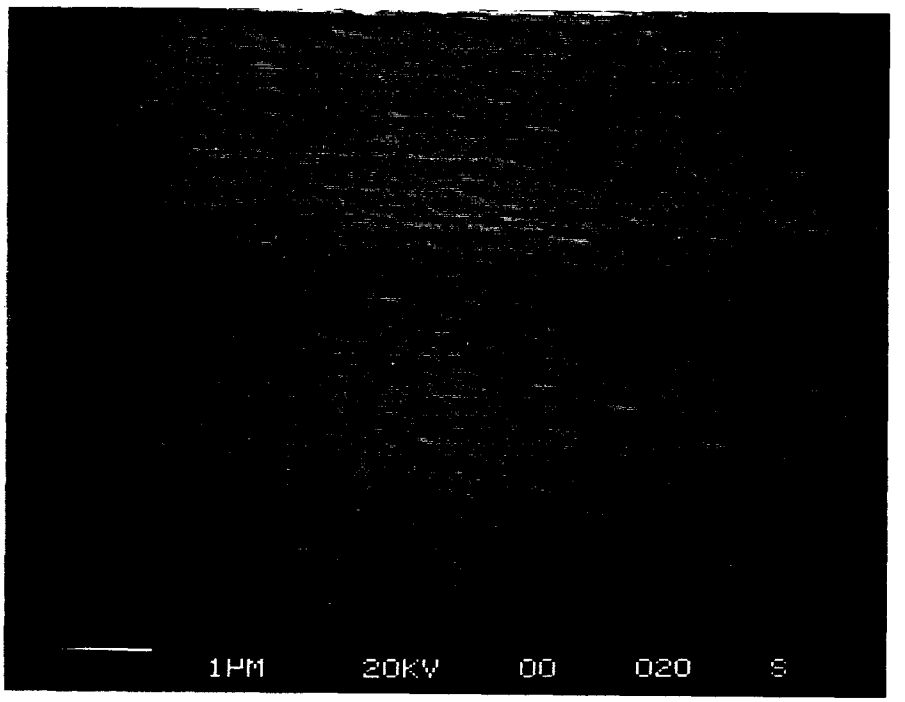

Figure 8. SEM photograph of ZnS surface from Growth Run #8 at glancing incidence.

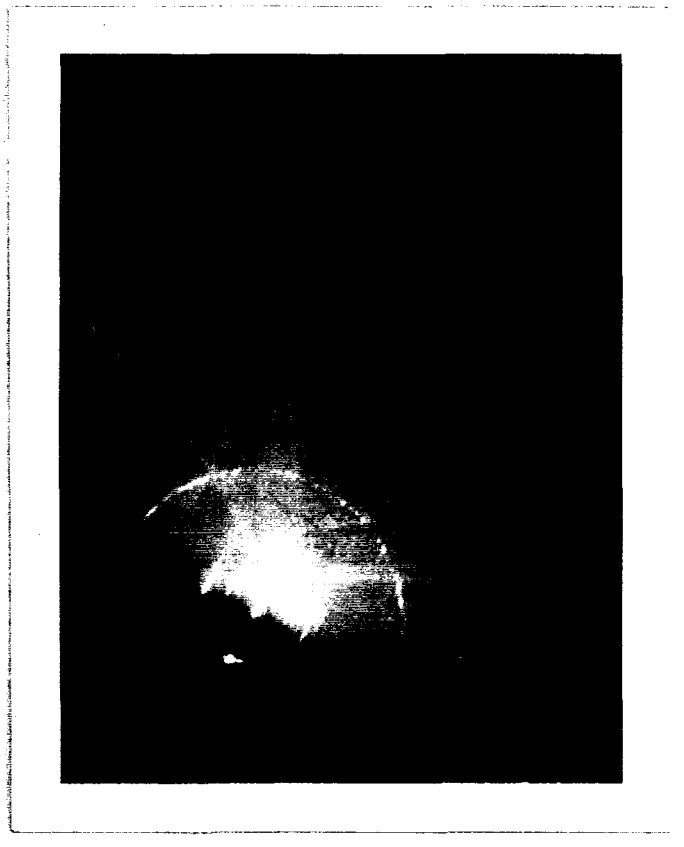

Figure 9. RHEED pattern of the (111)-oriented Si (7x7) surface reconstruction.

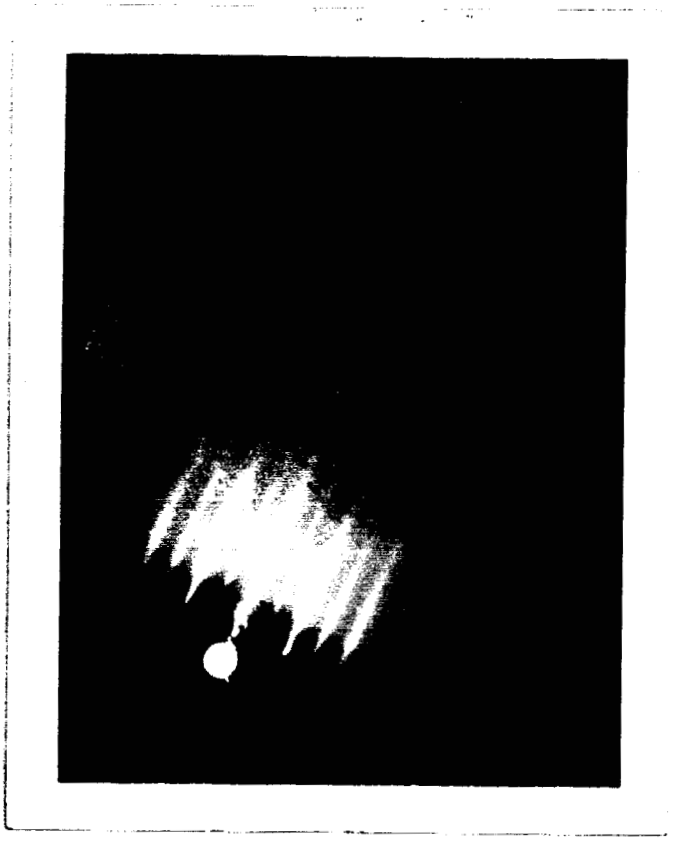

Figure 10. RHEED Pattern of the (111)-oriented Si (2x2) surface reconstruction due to impinging Zn and S_2 fluxes.